nature portfolio

Peer Review File

Lead carboxylates passivation for meter-scale perovskite solar modules

Corresponding Author: Professor Hairen Tan

Any redactions in this file are there to maintain patient confidentiality, the confidentiality of unpublished data, or to remove third-party material.

This file contains all reviewer reports in order by version, followed by all author rebuttals in order by version.

Version 0:

Reviewer comments:

Referee #1

(Remarks to the Author)
General Remarks
This manuscript reports an innovative surface passivation strategy using lead carboxylate derivatives (LCPs) and successfully demonstrates meter-scale perovskite solar modules with commercial potential. The authors achieve enhanced power conversion efficiency (PCE) while showcasing excellent module stability, with particularly impressive data from outdoor empirical testing. The successful translation of a laboratory scale, small area passivation technique to meter scale, large area processing represents a critical step toward the industrialization of perovskite photovoltaics. The manuscript is logically structured, supported by comprehensive experimental data, and excels in both academic depth and industrial application value. Nevertheless, to meet Nature's rigorous demands for scientific rigor and mechanistic depth, the authors need to address the following core issues through additional explanations or experimental revisions.

Detailed Comments
1. The interpretation of the crystallographic orientation in Figure 1e requires more caution. The perovskite film prepared using the high SVP solvent system does not exhibit a significant preferred orientation of the (100) plane. We suggest that the authors avoid potentially misleading terms related to "orientation" and instead more accurately describe the film's crystallinity and microstructural features.

2. The authors postulate the construction of an FAI terminated perovskite surface, but direct experimental evidence for this claim is currently lacking. We recommend that supplementary surface sensitive characterizations (e.g., angle resolved X ray photoelectron spectroscopy (ARXPS), high resolution XPS peak fitting, or first principles calculations combined with surface sensitive techniques) be performed to confirm the specific stoichiometry and atomic arrangement at the interface.

3. Supplementary Fig. 36 shows that the film surface becomes markedly smoother after LCP treatment, indicating that LCP induces surface reconstruction and acts as a "surface polishing" agent. Please clarify: to what extent does the significant improvement in device performance originate from this morphological smoothing, as opposed to purely electrical passivation at the interface?

4. Given the excellent module stability demonstrated in this work, encapsulation technology plays a crucial role. To ensure the reproducibility of this technical strategy within the community, we suggest that the authors further disclose the detailed encapsulation procedures and specific parameters for their large area modules, for example, by providing a supplementary video or a detailed flowchart, to facilitate replication by readers.

5. The authors observe that the LCP passivator diffuses into the bulk of the perovskite. In the perovskite field, conventional surface passivators are typically confined to the interface, whereas diffusion into the bulk implies a high dynamic mobility of these molecules. Please explain: does this molecular instability (i.e., ease of movement) contradict the observed long term operational stability? Furthermore, discuss the potential impact of such diffusion on charge transport and the chemical potential distribution within the device.

6. To further highlight the broad applicability of the LCP passivation strategy, we suggest that the authors test its performance in other bandgap systems – for example, its passivation effect in wide bandgap perovskite cells. Such validation would significantly enhance the generalizability and impact of the conclusions presented in this work.

Referee #2

(Remarks to the Author)
This manuscript reports a significant breakthrough in the industrialization of perovskite solar modules. The authors cleverly addressed the long-standing incompatibility between lab scale ammonium halide passivators and large-area fabrication under ambient conditions. The authors achieved this via a dual strategy: engineering an FAI rich surface using a rationally designed high SVP solvent system and then reacting it with a chemically robust lead carboxylate (Pb(OA)2). This approach is both scientifically insightful and practically impactful. The certified module efficiency of 22.0% (0.72 m2, total area) represents the highest reported values for commercially viable perovskite PV module to date. Overall, this work is of high impact and great interest for a broad community by providing in-depth insights. I believe this work represents a significant milestone towards highly efficient, stable, and cost-effective perovskite solar modules fully using scalable fabrication techniques. Therefore, I would recommend publication of this work in Nature after addressing the following minor issues/comments.
1.Figs. 2c and 2d present stability data under damp heat conditions, which is valuable. To provide a more comprehensive assessment of the LCP strategy's environmental robustness, it is recommended to also evaluate its UV light stability. UV induced degradation is a critical failure mode for perovskite photovoltaics.
2.The manuscript states that the commercial-scale perovskite modules are fabricated in ambient air. It is important to clarify the air-exposure tolerance of the two strategies before subsequent back-end processing (e.g., C60 evaporation, ALD SnO2 and electrode). Specifically, if the freshly deposited perovskite layers are deliberately aged in air for a defined period prior to continue the subsequent deposition, how significantly does this delay impact the final module performance? Quantifying this effect would be highly relevant for assessing the robustness and practical feasibility of the proposed fabrication routes in industrial settings.
3.The assertion in the paragraph titled "The formation of FAI-enriched surface…" that FAI is selectively carried to the top surface lacks sufficient theoretical justification and experimental evidence. Please provide a more detailed mechanistic explanation, supported by relevant data or references. Furthermore, the reasoning appears specific to FAI; please clarify why other constituent materials (e.g., PbI2, Cs+) do not exhibit similar surface-enrichment behavior under the same processing conditions.
4.The novelty of the claim regarding high-SVP solvents enabling surface customization via VCD is unclear. Please provide references to support its originality or clarify how it differs from prior work.
5.Regarding Fig. 2b, the authors note a coffee-ring effect after AHP treatment. While the PL mapping indicates spatial inhomogeneity, additional experimental evidence (e.g., optical microscopy, or SEM surface imaging) would strengthen this observation. Furthermore, the underlying causes of this effect should be discussed.
6.In the reliability section, providing the evolution of VOC, JSC, and FF before and after aging, rather than only normalized PCE, would offer deeper insight into whether the benefit of LCP mainly arises from reduced recombination, suppressed resistance buildup, or improved carrier collection.
7.The reported IEC 61215-related reliability results are impressive. A clearer summary table listing the conditions, endpoints, and evaluation criteria for each sub-test would improve readability.
8.It would be useful to briefly comment on the main source of efficiency loss when scaling from 810 cm2 to 0.72 m2, for example in terms of geometric fill factor, interconnection loss, or large-area uniformity.
9.The authors should add a conclusion section that clearly discusses the industrial feasibility of this method. Additionally, future perspectives on the design of more robust and versatile passivation strategies for perovskite solar cells should be provided. This addition would significantly strengthen the paper's completeness and practical relevance.

Referee #3

(Remarks to the Author)
Xu et al. report perovskite modules with high efficiency and durability by fabricating FACs-based perovskite films with an FAI-rich surface via a vacuum chamber drying (VCD) process using a solvent combination with high saturation vapor pressure (HSVP), and subsequently passivating this surface with $Pb(OA)_2$. The buried interface was treated in the same manner as in conventional approaches using MeO-4PACz, while for the top surface, instead of using alkyl ammonium halides (AHP, including RP and DJ types) to compensate for A-site deficiency, the authors treated the FAI-rich surface with $Pb(OA)_2$. This appears to be a reasonable approach, and the role of this strategy seems to have been relatively well elucidated through model experiments.
From the perspective of commercialization of perovskite solar modules, this work appears to be part of the continuum of solvent formulation development for large-area processing using slot-die coating. In particular, the study is evaluated as providing a meaningful research direction for the community by proposing a surface passivation strategy that can overcome the durability issues associated with conventional AHP-based surface treatments. Therefore, the manuscript could be considered for publication if the following comments are adequately addressed.
1. For the VCD process, the authors selected an HSVP solvent combination of 2-ME, DOL, and DMSO, and the role of DOL in securing the shelf life of the perovskite ink appears to have been well investigated. However, while the solvent properties of 2-ME and DMSO are presented, it seems necessary to also provide the solvent properties of DOL, including vapor pressure and solubility.

2. From the perspective of large-area thin-film processing, studies on FACs-based perovskite inks using solvent combinations such as 2-ME, DMSO, or NMP have already been reported in the literature. In this work, the key differentiation appears to lie in the use of DOL. The role of DOL seems similar to that of 2-Me–THF previously reported by the same group. Therefore, it would be helpful if the authors comment on the specific reason for selecting DOL in this study and what limitations may arise when using 2-Me–THF.
3. In general, since the solubility of FAI in solvents used for dissolving perovskites is much higher than that of PbI_2, it is thermodynamically expected that a PbI_2-rich surface forms. To address this, it is commonly known that a slight excess of A-site precursors is added during perovskite film fabrication. In this context, it seems possible that an FAI-rich perovskite film could also be obtained by initially introducing excess A-site (FAI) in this work. Therefore, it would be beneficial to examine what happens when excess FAI is used.
4. In the current manuscript, only two cases are compared: $Pb(OA)_2$ treatment on perovskite films prepared using HSVP solvents, and AHP treatment on films prepared using LSVP solvents. It would be helpful to examine what happens when AHP is applied to perovskite films prepared using HSVP solvents.
5. In this study, $EDAI_2$ is used as an example of AHP. However, based on previous reports from the same group, AHPs such as TAC are expected to produce surfaces with hydrophobicity comparable to that of $Pb(OA)_2$. Therefore, it would be more appropriate to compare $Pb(OA)_2$ with AHP systems that exhibit similar hydrophobicity in order to better demonstrate the advantages of $Pb(OA)_2$.
6. The proposed reaction mechanism, in which $Pb(OA)_2$ reacts with 2FAI to form 2OA–FA and PbI_2, followed by the reaction of PbI_2 with FAI to form $FAPbI_3$, appears reasonable. However, there seems to be insufficient evidence that nano-sized α-$FAPbI_3$ is formed and that OA passivates both the surface and grain boundaries when $Pb(OA)_2$ is applied to an FAI-rich perovskite film. While changes in the surface are indirectly demonstrated through SEM images and KPFM analysis, evidence regarding changes at grain boundaries appears to be lacking. Therefore, it would be helpful to provide additional analyses focusing on grain boundaries, such as KPFM comparisons between control and target samples.
7. Overall, it appears that both efficiency and durability are improved through the solvent formulation and $Pb(OA)_2$ passivation. It is expected that similar improvements would also be observed at the unit-cell level. For the benefit of readers, it would be helpful to present how the performance of unit devices changes compared to conventional recipes.
8. Finally, in order to enable reproducibility of the experiments, it would be beneficial to provide a more detailed description of the module fabrication process. In addition, it would be helpful to include cross-sectional SEM images as well as SEM images and specifications of P1, P2, and P3 patterning.

Version 1:

Reviewer comments:

Referee #1

(Remarks to the Author)
The authors have addressed most of my previous concerns, and I believe that the scientific quality and overall presentation of the manuscript now meet the publication standard of Nature. In my view, this work represents a significant milestone towards highly efficient, stable, and cost-effective perovskite solar modules fabricated entirely using scalable manufacturing techniques. Therefore, I recommend publication in Nature after the authors address the following minor comment.

Comment: The modules presented in this work employ a standalone NiOx hole-transport layer (Supplementary Fig. 16). Given that state-of-the-art perovskite solar cells commonly utilize NiOx/SAM or SAM-based hole-selective contacts to maximize device performance, the authors should clarify the rationale for adopting standalone NiOx in this study and explain why NiOx/SAM or SAM architectures were not pursued. In addition, it would be valuable to discuss the key challenges associated with implementing SAMs in large-area module fabrication and to clarify how this design choice relates to the high module performance reported in this work.

Referee #2

(Remarks to the Author)
The manuscript has been well revised and it could be accepted as is.

Referee #3

(Remarks to the Author)
The authors have thoroughly and satisfactorily addressed all the reviewers' comments and concerns. The revisions made have significantly strengthened the manuscript. In this regard, I recommend this manuscript to be accepted as it is.
(Only one minor correction: In the Nernst–Einstein relation equation, B should be subscript in kB)

Point-to-Point Response to the Reviewers' Comments

Manuscript #: 2026-03-08492

We thank the reviewers for their constructive feedback and for recognizing the significance of this work. We have carefully revised the manuscript to address all comments in detail. Reviewer comments are presented in black, our responses are provided in blue, and the revised text in the manuscript is presented in boxes. All modifications in the revised manuscript have been clearly highlighted.

Referee #1 (Remarks to the Author):

General Remarks

This manuscript reports an innovative surface passivation strategy using lead carboxylate derivatives (LCPs) and successfully demonstrates meter-scale perovskite solar modules with commercial potential. The authors achieve enhanced power conversion efficiency (PCE) while showcasing excellent module stability, with particularly impressive data from outdoor empirical testing. The successful translation of a laboratory scale, small area passivation technique to meter scale, large area processing represents a critical step toward the industrialization of perovskite photovoltaics. The manuscript is logically structured, supported by comprehensive experimental data, and excels in both academic depth and industrial application value. Nevertheless, to meet Nature's rigorous demands for scientific rigor and mechanistic depth, the authors need to address the following core issues through additional explanations or experimental revisions.

Response: We thank the reviewer for the appreciation of our work and the constructive suggestions to improve the manuscript.

Detailed Comments

1. The interpretation of the crystallographic orientation in Figure 1e requires more caution. The perovskite film prepared using the high SVP solvent system does not exhibit a significant preferred orientation of the (100) plane. We suggest that the authors avoid potentially misleading terms related to "orientation" and instead more accurately describe the film's crystallinity and microstructural features.

Response: We thank the reviewer for the valuable suggestion. Now we revised the interpretation in the manuscript as follows:

> "*Grazing incidence wide-angle X-ray scattering (GIWAXS) at 0.4° indicated that the perovskite film fabricated using the high-SVP solvent showed dominant diffraction features associated with the (100) plane, accompanied by reduced diffuse scattering*[37]. *In contrast, the film formed with the low-SVP solvent showed significant* PbI_2 *residue and the presence of the photo-inactive δ-phase perovskite (Fig. 1e, Supplementary Fig. 25).*"

2. The authors postulate the construction of an FAI terminated perovskite surface, but direct experimental evidence for this claim is currently lacking. We recommend that supplementary surface sensitive characterizations (e.g., angle resolved X ray photoelectron spectroscopy (ARXPS), high resolution XPS peak fitting, or first principles calculations combined with surface sensitive techniques) be performed to

confirm the specific stoichiometry and atomic arrangement at the interface.

Response: We appreciate this insightful comment regarding the direct experimental evidence to support the FAI-terminated perovskite surface. We fully agree that confirming the specific stoichiometry at the interface is essential. In response, we performed high-resolution XPS depth-profile measurements to probe the near-surface elemental composition and chemical states. Although the current experimental setup limits our ability to derive an exact atomic stoichiometric ratio solely from XPS, the data clearly demonstrate the enrichment of FAI-related species (FA^+ and I^-) at the top surface, which is consistent with our hypothesis. Furthermore, we incorporated relevant first principles calculations that reveal a stronger interaction between 2-Me and FAI, indicating that 2-Me facilitates the transport of FAI to the perovskite surface during the rapid concentration and evacuation process.

We now revised the manuscript as follows:

"*X-ray photoelectron spectroscopy (XPS) showed that the high-SVP perovskite surface exhibits binding energies (I 3d, N 1s) nearly identical to bare FAI, while its bulk characteristics resemble those of the low-SVP perovskite (Fig. 1d, Supplementary Fig. 13); this indicates that the FA^+ and I^- ions reside in an essentially uncoordinated state at the surface.*"

"*The formation of the FAI-enriched surface is attributed to the vacuum-induced directional migration of solvent from the film interior toward the upper surface, which drives convective transport and facilitates the accumulation of solute (FAI) on the wet perovskite film (Supplementary Fig. 14). This directional solvent flow entrains a high concentration of dissolved FAI toward the liquid-air interface, thereby inducing supersaturation and subsequent precipitation. Crucially, this directional co-transport is significantly enhanced by the strong hydrogen-bonding interactions between 2-Me and FAI (Supplementary Fig. 15), providing a mechanistic rationale for the preferential surface enrichment.*"

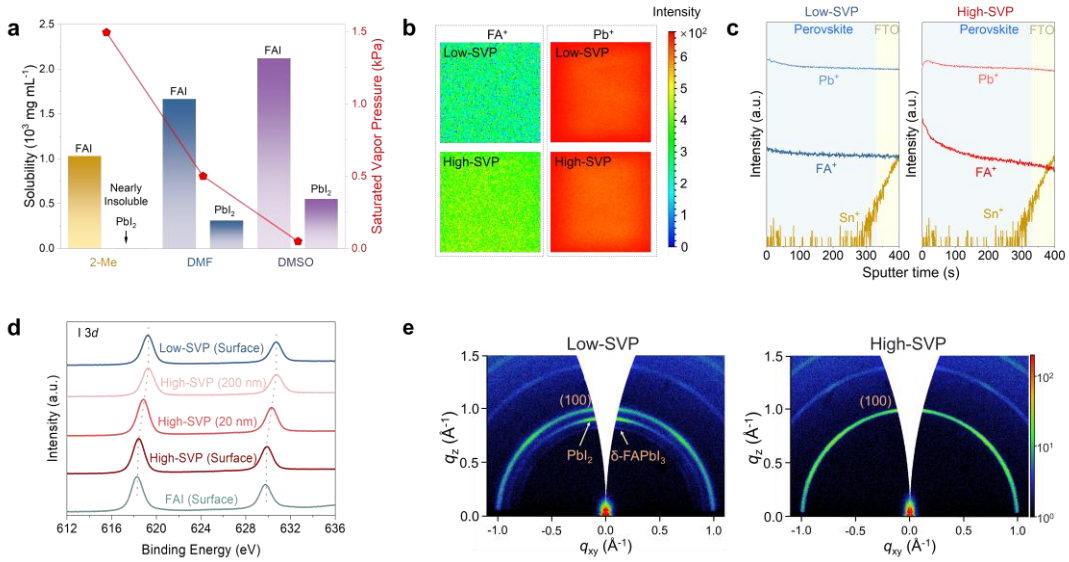

Fig. 1 | Surface states of perovskite films. a, Solubility of FAI and PbI_2 in 2-Me, DMF, and DMSO, and the saturated vapor pressure of these solvents at room temperature. **b,** TOF-SIMS surface ion mapping of the FA^+ and Pb^+ on the low-SVP and high-SVP prepared perovskite films. **c,** TOF-SIMS depth profile of the perovskite films. **d,** I 3*d* XPS spectra of pristine FAI, and perovskite films prepared from low-SVP and high-SVP solvent systems. **e,** GIWAXS patterns of the perovskite films prepared by low-SVP and high-SVP.

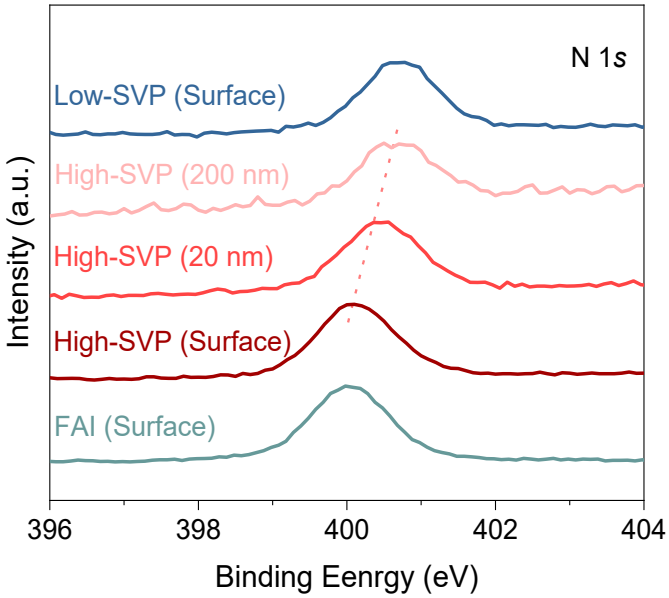

Supplementary Fig. 13 | XPS spectra. N 1*s* XPS spectra of FAI powder and perovskite films fabricated using low-SVP and high-SVP solvents. Measurements for FAI and the low-SVP perovskite were confined to the top surface, while those for the high-SVP perovskite included the top surface and depths of 20 nm and 200 nm.

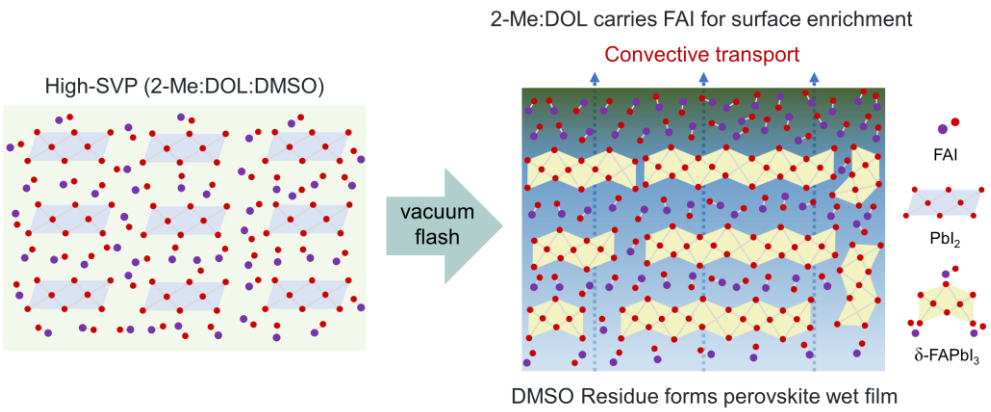

Supplementary Fig. 14 | The schematic illustration of the dynamic process of the surface enrichment of FAI during VCD processing. The high SVP characteristic of 2-Me induces its rapid evaporation under vacuum conditions. This establishes a steep concentration gradient and intense Marangoni flow, thereby driving the migration of FAI toward the liquid–air interface. Owing to the kinetic trapping effect during rapid solvent removal (where the solvent evaporation rate far exceeds the solute diffusion rate, causing FAI transported to the interface to be trapped by the rapidly forming solid perovskite matrix before redistributing into the bulk), FAI species are preferentially accumulated and stabilized at the perovskite surface, ultimately forming an FAI-enriched termination layer.

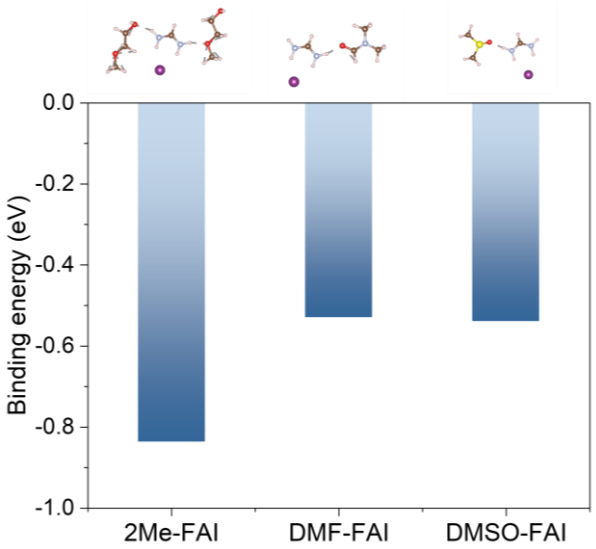

Supplementary Fig. 15 | Binding energy calculations of FAI and solvents. The 2-Me exhibits a higher binding energy with FAI compared to DMF or DMSO. This indicates a stronger interaction between 2-Me and FAI, suggesting that 2-Me forms more favorable associations with FAI species.

3. Supplementary Fig. 36 shows that the film surface becomes markedly smoother after LCP treatment, indicating that LCP induces surface reconstruction and acts as a

"surface polishing" agent. Please clarify: to what extent does the significant improvement in device performance originate from this morphological smoothing, as opposed to purely electrical passivation at the interface?

Response: We appreciate this insightful question regarding the relative contributions of morphological smoothing versus electrical passivation. We conducted a systematic analysis to distinguish these two effects. The results demonstrate that the electrical passivation afforded by the LCP strategy is the primary factor responsible for the observed enhancements in device performance.

To elucidate the relationship between surface morphology and device performance, we employed ammonium salts with hydrophobic structures analogous to $Pb(OA)_2$, specifically, trimethyltetradecylammonium chloride (TAC) and oleylamine hydrochloride (OAC), as alternative surface modifiers (Supplementary Fig. 83). Notably, TAC and OAC resulted in significant morphological variations on the perovskite surface, accompanied by blurred grain boundaries (Supplementary Fig. 85), yet the resulting modules still exhibited enhanced efficiencies (Supplementary Fig. 87). This apparent contradiction confirms that electrical passivation at the interface, rather than morphological smoothing, plays the pivotal role in performance enhancement.

On the other hand, when the low-SVP perovskite was treated with the $Pb(OA)_2$ passivator, the surface roughness showed minimal change (Fig. R1), yet the module efficiency exhibited a slight decline. The detailed parameters indicate a marginal increase in V_{OC} but a decrease in FF (Fig. R2). This can be interpreted as follows: the introduced oleate (OA^-) ions at the low-SVP perovskite surface provide a certain degree of interfacial passivation, while the uncoordinated, free $Pb(OA)_2$ species concurrently form a resistive interface that impedes charge transport.

We now revised the manuscript as follows:

"*We further evaluated the PCEs and reliability of AHP systems exhibiting hydrophobicity comparable to that of LCP (Supplementary Note 8, Supplementary Figs. 83–88), thereby validating the advantages of the LCP strategy.*"

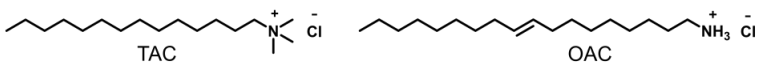

Supplementary Fig. 83 | Molecular Structures of TAC and OAC.

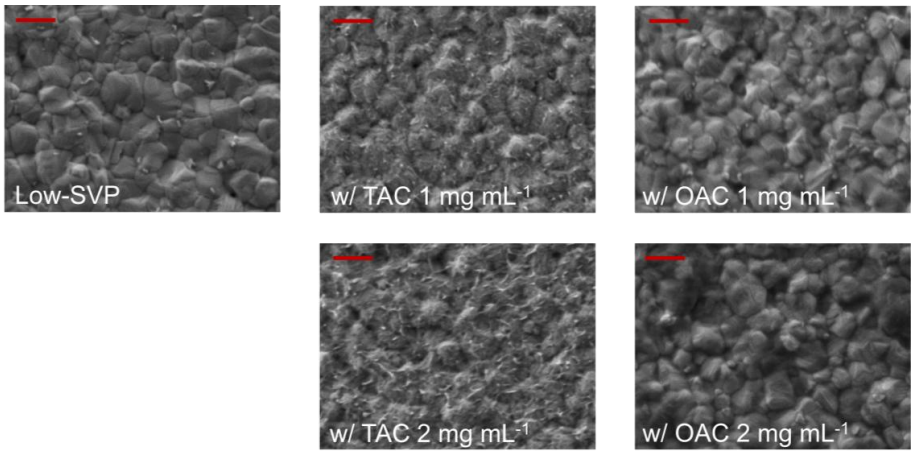

Supplementary Fig. 85 | SEM images of low-SVP perovskite films. The top-view SEM images of low-SVP perovskite film with TAC and OAC passivation. The scale bars correspond to 1 μm in all images.

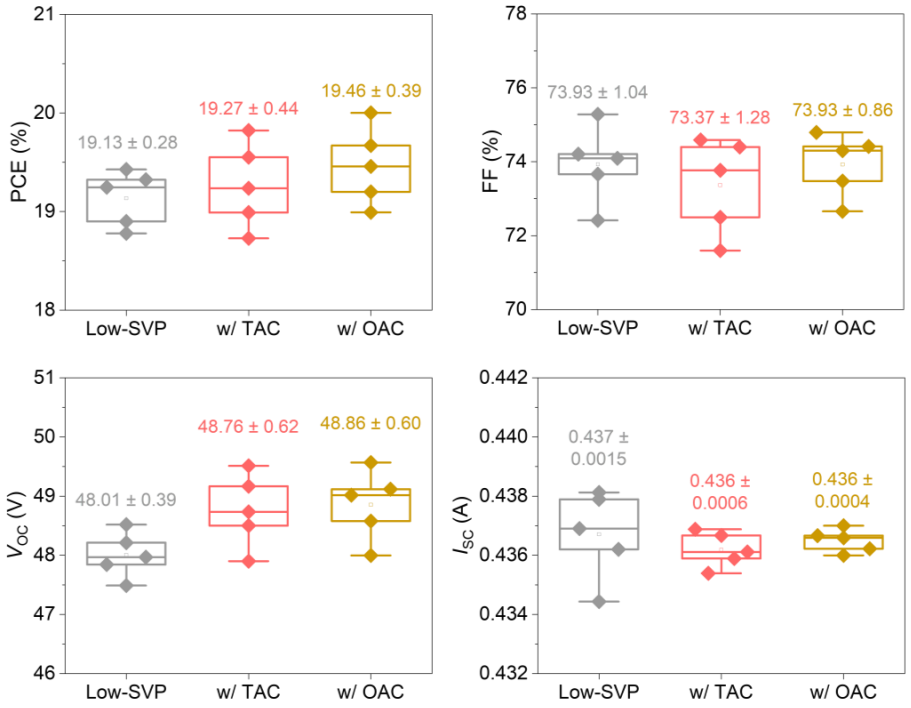

Supplementary Fig. 87 | Statistical photovoltaic parameters of the modules. The PV modules fabricated by low-SVP perovskite films with TAC and OAC. The aperture area of the module is 810 cm^2. Five parallel data sets were taken for each set of conditions. Scatters represent raw data; boxplots show the interquartile range with the median as the center line; whiskers indicate the 5th–95th percentiles. Numerical data are presented as mean ± SD.

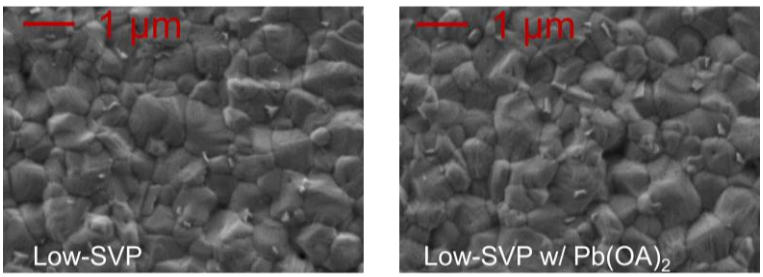

Fig. R1 | SEM images of low-SVP perovskite films. The top-view SEM images of low-SVP perovskite film with $Pb(OA)_2$ passivation.

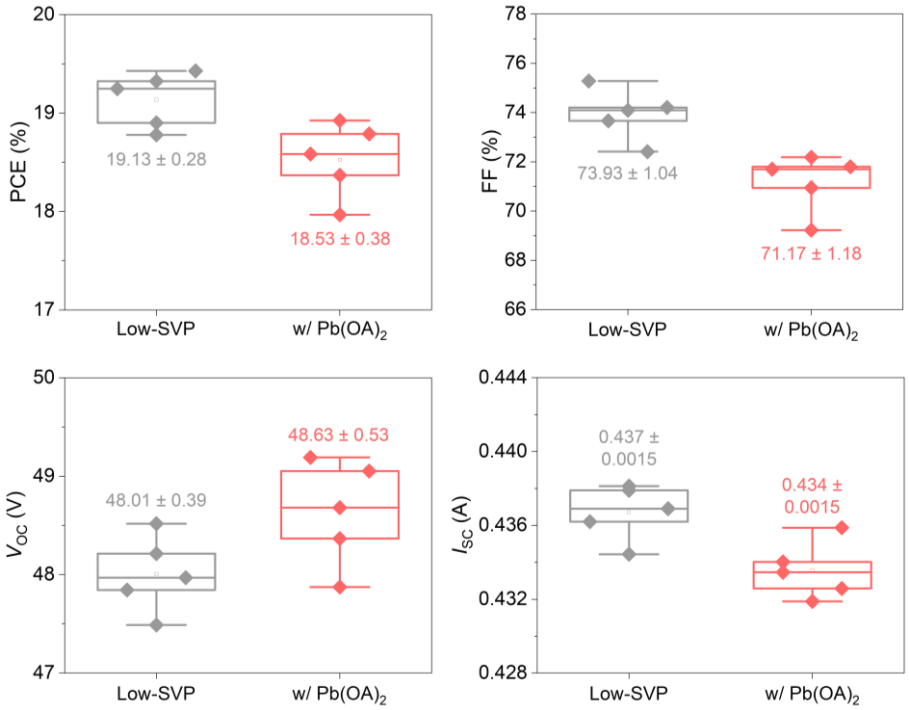

Fig R2 | Statistical photovoltaic parameters of the modules. The PV modules fabricated by low-SVP perovskite films with 1 mg mL^{-1} $Pb(OA)_2$. The aperture area of the module is 810 cm^2. Five parallel data sets were taken for each set of conditions. Scatters represent raw data; boxplots show the interquartile range with the median as the center line; whiskers indicate the 5th–95th percentiles. Numerical data are presented as mean ± SD.

4. Given the excellent module stability demonstrated in this work, encapsulation technology plays a crucial role. To ensure the reproducibility of this technical strategy within the community, we suggest that the authors further disclose the detailed encapsulation procedures and specific parameters for their large area modules, for example, by providing a supplementary video or a detailed flowchart, to facilitate replication by readers.

Response: We appreciate the comment highlighting the critical role of encapsulation

in ensuring the excellent module stability demonstrated in this work. We added a supplementary note to describe the entire fabrication procedures with encapsulation steps in the revised Supplementary Information:

*"**Supplementary Note 2:***

PV modules fabrication

A busbar was attached to the metal electrodes to facilitate electrical testing. The module edges were sealed with butyl rubber, and a polyolefin elastomer (POE) encapsulation film was applied over the active area. A glass cover of the same dimensions as the substrate was placed on top of the butyl rubber and POE stack. The assembly was laminated at 130 °C for 10 minutes. Following lamination, the perovskite solar module was ready for stability testing. Finally, a junction box was installed to enable series interconnection with adjacent modules, forming a panel suitable for photovoltaic power-station deployment."

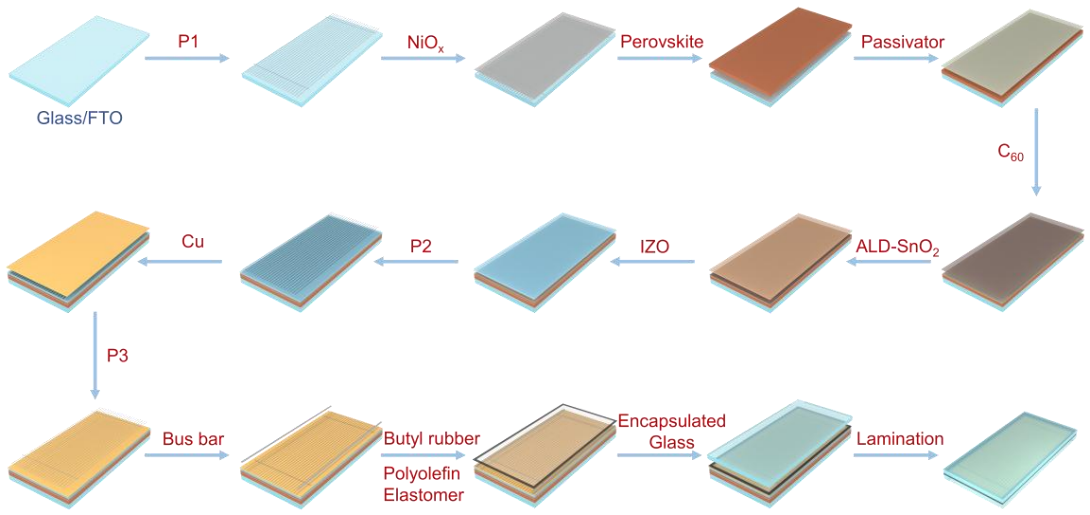

Supplementary Fig. 16 | Process flow diagram for the fabrication of PV modules

5. The authors observe that the LCP passivator diffuses into the bulk of the perovskite. In the perovskite field, conventional surface passivators are typically confined to the interface, whereas diffusion into the bulk implies a high dynamic mobility of these molecules. Please explain: does this molecular instability (i.e., ease of movement) contradict the observed long term operational stability? Furthermore, discuss the potential impact of such diffusion on charge transport and the chemical potential distribution within the device.

Response: We thank the reviewer for raising this important and insightful point regarding the observed diffusion behavior of the LCP passivator and its implications for stability and device physics. Here, we performed TOF-SIMS analysis and DFT

calculations to investigate the distribution and binding behavior of OA^- in perovskites. We found that OA^- is mainly localized at the film surface with minimal bulk penetration (Supplementary Fig. 48), and once it occupies iodine vacancy sites, it exhibits a higher binding energy than native I^-, which does not compromise the film's inherent stability (Supplementary Fig. 47). According to the ion migration activation energy of perovskite films, we added a note in supplementary information by performing temperature-dependent conductivity, potential distribution after etching of perovskite films and provided a comprehensive discussion in the revised manuscript:

"*Density functional theory (DFT) calculations indicated that OA^- primarily adsorbs at iodine vacancy sites on the perovskite surface to coordinate with undercoordinated lead, and simultaneously binds to FA^+ cations through hydrogen bonding (Fig. 3b). This adsorption configuration exhibits a higher binding energy than that of I^- at the same sites (Supplementary Fig. 47). The distribution of OA^- in the 3-dimensional depth profile of COO^+, as measured by TOF-SIMS, showed that the oleate was predominantly localized at the film surface, with only trace amounts penetrating into the perovskite bulk via grain boundaries (Supplementary Fig. 48). The measured activation energy (E_a) and cross-sectional potential difference of the perovskite film confirm that this passivation strategy does not adversely affect ion migration within the film (Supplementary Note 5, Supplementary Figs. 49–51).*"

"***Supplementary Note 5:***

The ion migration activation energy of perovskite film.

Herein, we investigated the ion migration properties of the perovskite films using temperature-dependent conductivity measurements on Au/perovskite/Au structures to experimentally determine the ion migration activation energy (E_a). The activation energy can be extracted by fitting the raw data to the Nernst–Einstein relation:

$$\sigma(T)=\frac{\sigma 0}{T} exp\ (\frac{Ea}{kBT})$$

where $\sigma(T)$ is the conductivity as a function of temperature, σ_0 is a temperature-independent prefactor, and k_B is the Boltzmann constant.

The fitted Arrhenius plots exhibit two distinct linear regimes. In the low-temperature regime, ion migration is essentially suppressed due to insufficient thermal energy. Above a critical temperature, ion migration becomes thermally activated, leading to an exponential enhancement in conductivity.

From the slopes of the Arrhenius plots, the ion migration activation energy of the high-SVP perovskite film was determined to be 0.531 eV, which increased slightly to

0.554 eV after LCP passivation (Supplementary Fig. 49). This small but clear gain in indicates that the LCP passivation strategy moderately suppresses ion migration, a conclusion that aligns with the theoretical calculations presented in Supplementary Fig. 47.

Furthermore, we employed a quasi-in situ FIB-SEM-AFM technique to analyze the cross-sectional morphology and potential distribution. Supplementary Fig. 50a provides a schematic of the sample preparation, Supplementary Fig. 50b shows a photograph of the FIB etching setup, and Supplementary Fig. 50c presents an SEM image of the intermediate layer exposed after FIB etching on the high-SVP perovskite surface. Theoretically, if OA^- were to infiltrate the perovskite bulk along grain boundaries, a potential difference between the grain boundaries and grain interiors would be expected. However, the actual measurements reveal no significant potential contrast between the grain boundaries and the interiors in the micro-region corresponding to Supplementary Fig. 51. We attribute this to the extremely low concentration of OA^- that permeates into the bulk via grain boundaries, resulting in a negligible change in chemical potential. Additionally, the grain-boundary gaps are highly compact, which may prevent KPFM from accurately resolving the subtle electrical signal variations within such confined areas. Therefore, the trace-level penetration of OA^- does not adversely affect charge transport or the chemical potential landscape within the film."

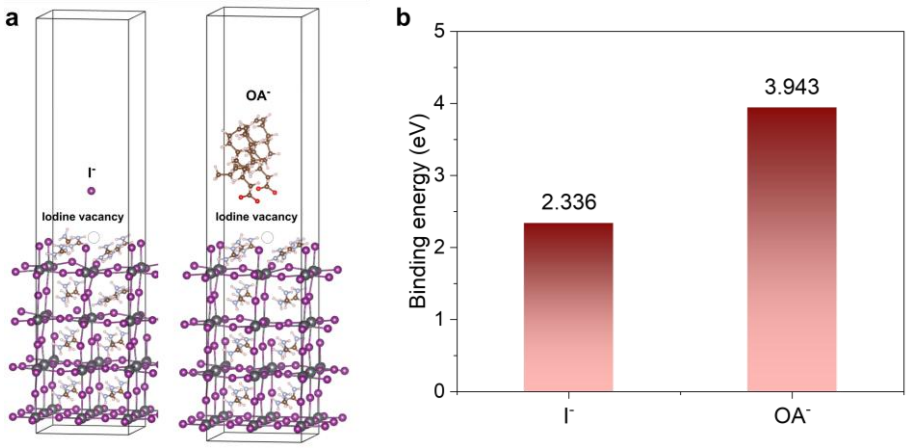

Supplementary Fig. 47 | Calculation of the binding energies of I^- and OA^- at iodine vacancy sites. a, Computational models of I^- and OA^- on a defective PbI-terminated surface (I^- vacancy). **b,** Binding energies of I^- and OA^- occupying iodine vacancies

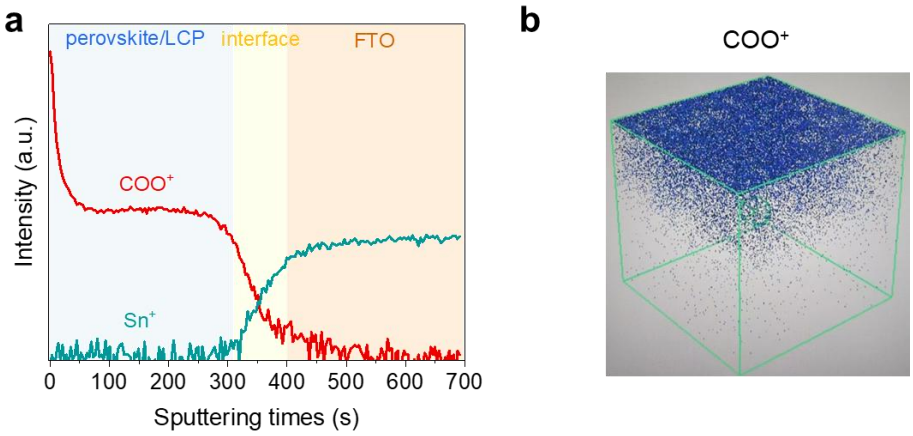

Supplementary Fig. 48 | The TOF-SIMS analysis of high-SVP perovskite film with LCP. **a,** TOF-SIMS depth profile and **b,** 3D distribution plot of the LCP-passivated perovskite film prepared via the high-SVP method.

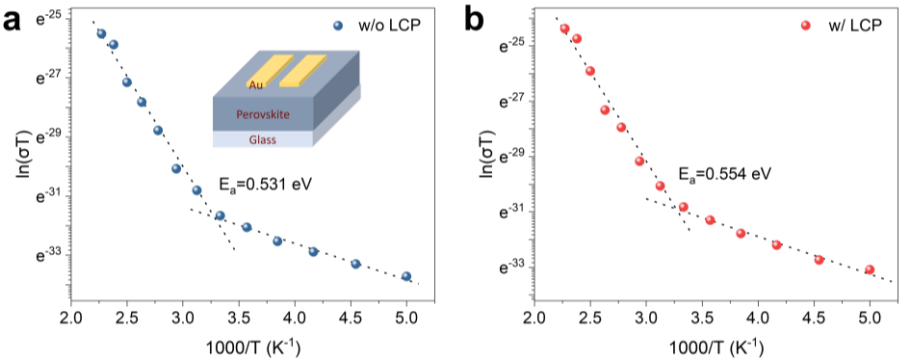

Supplementary Fig. 49 | Temperature-dependent conductivity of perovskite film. a, high-SVP perovskite film and **b,** high-SVP perovskite film w/ LCP.

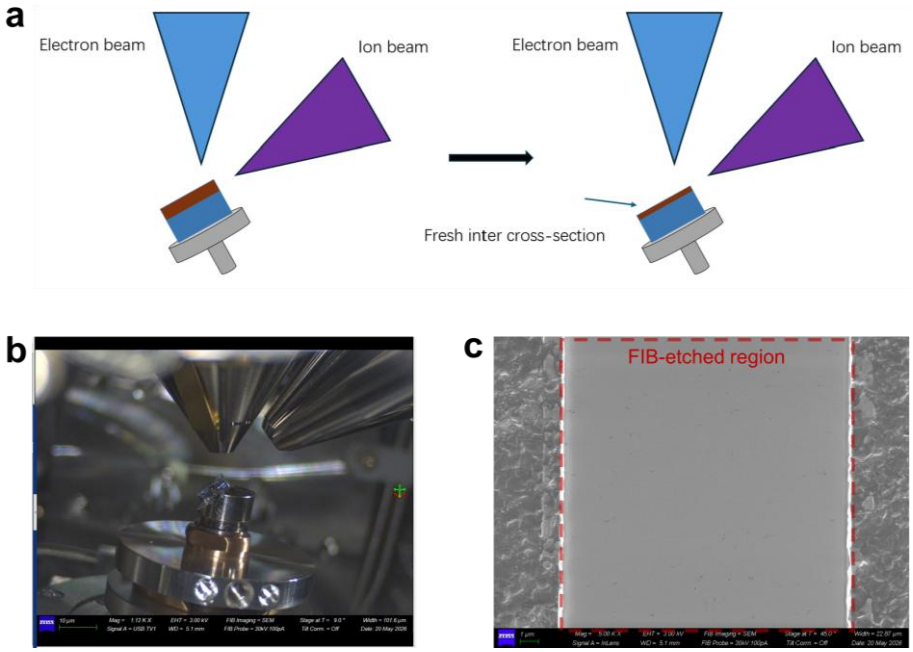

Supplementary Fig. 50 | Surface etching of perovskite film (high-SVP w/ LCP). a, Schematic illustration of focused ion beam (FIB) etching on a perovskite surface. **b,** Photograph of the surface etching setup. **c,** SEM image of the perovskite surface after etching, showing the exposed internal layer where the top surface has been removed in the central region.

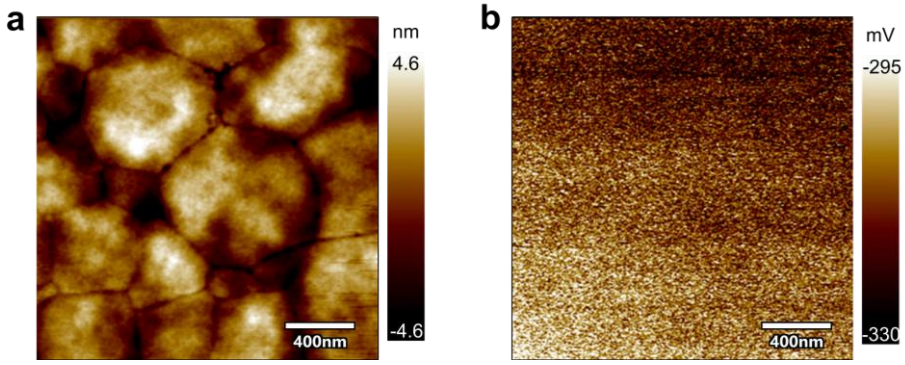

Supplementary Fig. 51 | Potential distribution of perovskite crystals after etching. a, The AFM image and **b,** corresponding KPFM image of high-SVP perovskite film with LCP. The measurement location corresponds to the region subjected to FIB etching in Supplementary Fig. 50c.

6. To further highlight the broad applicability of the LCP passivation strategy, we suggest that the authors test its performance in other bandgap systems – for example, its passivation effect in wide bandgap perovskite cells. Such validation would significantly enhance the generalizability and impact of the conclusions presented in this work.

Response: We appreciate this practical suggestion and have extended the LCP passivation strategy to wide-bandgap (WBG) perovskite cells to demonstrate its broad applicability. We supplemented two representative WBG perovskites with bandgaps of approximately 1.68 eV and 1.80 eV. Notable increases in both V_{OC} and FF were observed by incorporating the LCP strategy into these WBG systems. We believe this extension significantly enhances the universality of the strategy presented in this work.

We now revised manuscript and supplementary information as follows:

"*Moreover, this strategy demonstrates a universal efficiency improvement in wide-bandgap perovskite systems (1.68 eV and 1.80 eV) (Supplementary Figs. 67–70), which significantly enhances the generality and impact of the conclusions presented in this work.*"

Methods section:

"***$Cs_{0.05}MA_{0.05}FA_{0.90}Pb(I_{0.75}Br_{0.25})_3$ perovskite ink (1.68 eV)***

The perovskite powders including 312 mg CsI, 3715 mg FAI, 191 mg MAI, 6915 mg PbI_2, 3307 mg $PbBr_2$, 324 mg MACl were dissolved in mixed solvent (40 mL). The low-SVP solvent is composed of a mixture of DMF and DMSO (8:2, volume/volume). The high-SVP solvent is composed of a mixture of 2-Me, DOL, DMSO (5:3:2, volume/volume/volume). The ink was stirred at room temperature for at least 1 hour, then filtered through a 0.22 μm PTFE membrane before deposition.

$Cs_{0.15}FA_{0.85}Pb(I_{0.6}Br_{0.4})_3$ perovskite ink (1.80 eV)

The perovskite powders including 936 mg CsI, 3509 mg FAI, 4426 mg PbI_2, 5285 mg $PbBr_2$, 162 mg MACl were dissolved in mixed solvent (40 mL). The low-SVP solvent is composed of a mixture of DMF and DMSO (8:2, volume/volume). The high-SVP solvent is composed of a mixture of DMF, 2-Me, DOL, DMSO (1:4:3:2, volume/volume/volume/volume). The ink was stirred at room temperature for at least 1 hour, then filtered through a 0.22 μm PTFE membrane before deposition."

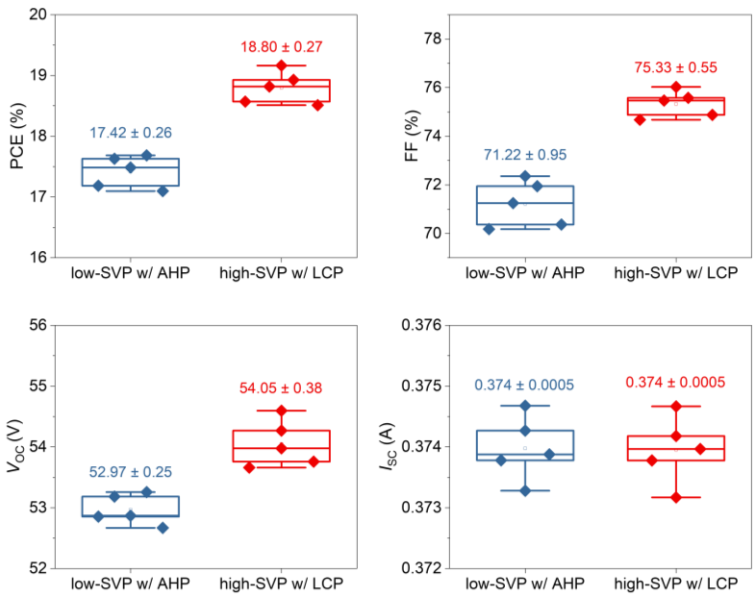

Supplementary Fig. 67 | Statistical photovoltaic parameters of the perovskite modules (The perovskite film bandgap is 1.68 eV). The PV modules fabricated by low-SVP perovskite with AHP and high-SVP perovskite with LCP. The aperture area of the module is 810 cm^2. Five parallel data sets were taken for each set of conditions. Scatters represent raw data; boxplots show the interquartile range with the median as the center line; whiskers indicate the 5th–95th percentiles. Numerical data are presented as mean ± SD.

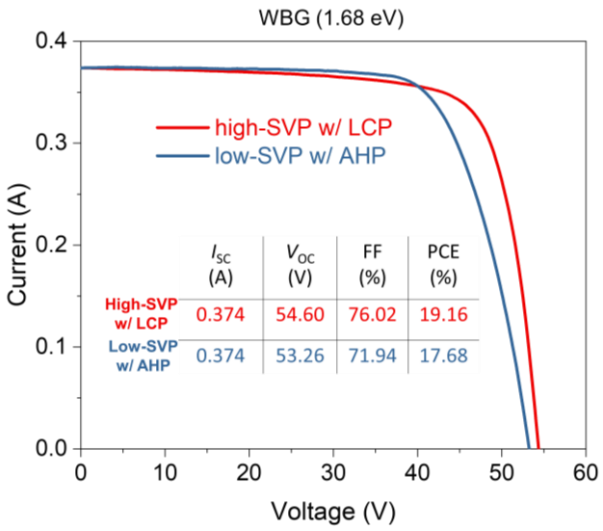

Supplementary Fig. 68 | *I-V* curves of the optimal modules (Bandgap=1.68 eV). The modules, fabricated from low-SVP perovskite with AHP and high-SVP perovskite with LCP, correspond to Supplementary Fig. 67.

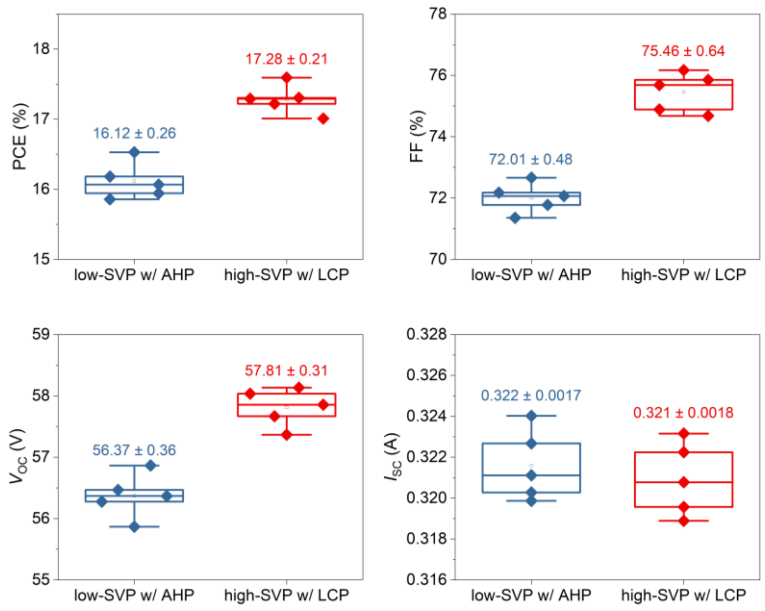

Supplementary Fig. 69 | Statistical photovoltaic parameters of the perovskite modules (The perovskite film bandgap is 1.80 eV). The PV modules fabricated by low-SVP perovskite with AHP and high-SVP perovskite with LCP. The aperture area of the module is 810 cm^2. Five parallel data sets were taken for each set of conditions. Scatters represent raw data; boxplots show the interquartile range with the median as the center line; whiskers indicate the 5th–95th percentiles. Numerical data are presented as mean ± SD.

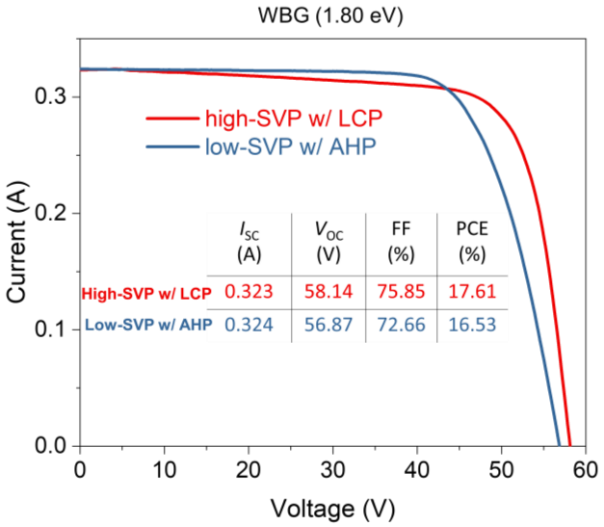

Supplementary Fig. 70 | *I-V* curves of the optimal modules (Bandgap=1.80 eV). The modules, fabricated from low-SVP perovskite with AHP and high-SVP perovskite with LCP, correspond to Supplementary Fig. 69.

Referee #2 (Remarks to the Author):

General Remarks

This manuscript reports a significant breakthrough in the industrialization of perovskite solar modules. The authors cleverly addressed the long-standing incompatibility between lab scale ammonium halide passivators and large-area fabrication under ambient conditions. The authors achieved this via a dual strategy: engineering an FAI rich surface using a rationally designed high SVP solvent system and then reacting it with a chemically robust lead carboxylate ($Pb(OA)_2$). This approach is both scientifically insightful and practically impactful. The certified module efficiency of 22.0% (0.72 m^2, total area) represents the highest reported values for commercially viable perovskite PV module to date. Overall, this work is of high impact and great interest for a broad community by providing in-depth insights. I believe this work represents a significant milestone towards highly efficient, stable, and cost-effective perovskite solar modules fully using scalable fabrication techniques. Therefore, I would recommend publication of this work in Nature after addressing the following minor issues/comments.

Response: We are grateful to the reviewer for the very supportive evaluation and for the valuable suggestions. We have carefully addressed all the points raised, as detailed in our responses below.

Detailed Comments

1. Figs. 2c and 2d present stability data under damp heat conditions, which is valuable. To provide a more comprehensive assessment of the LCP strategy's environmental robustness, it is recommended to also evaluate its UV light stability. UV induced degradation is a critical failure mode for perovskite photovoltaics.

Response: We appreciate the recommendation to further assess the environmental robustness of the LCP strategy. We have conducted additional stability tests under UV light exposure to complement the damp-heat data and provided a comprehensive discussion in the revised manuscript and supplementary information:

> *"X-ray diffraction (XRD) similarly revealed the LCP-modified perovskite films exhibited excellent environmental thermal and ultraviolet stability (Fig. 2d, Supplementary Figs. 43 and 44)."*

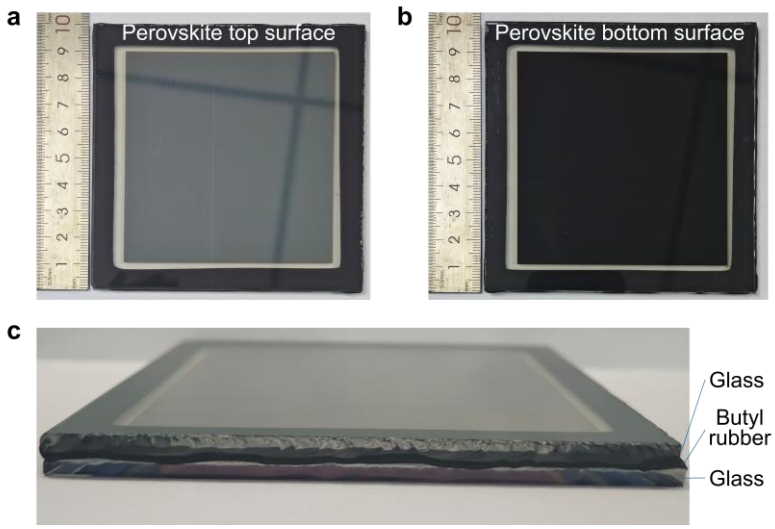

Supplementary Fig. 43 | Photograph of the perovskite film encapsulated in a glass-glass configuration. a, Perovskite film top surface. **b,** Perovskite film bottom surface. **c,** Photograph of the encapsulation cross-section. To exclude the influence of atmospheric conditions during UV aging, the perovskite films were encapsulated prior to aging. The edges were sealed with butyl rubber via lamination, while this encapsulation removed the polyolefin elastomer (POE) filler upon perovskite layer to enable subsequent characterization of the fractured samples.

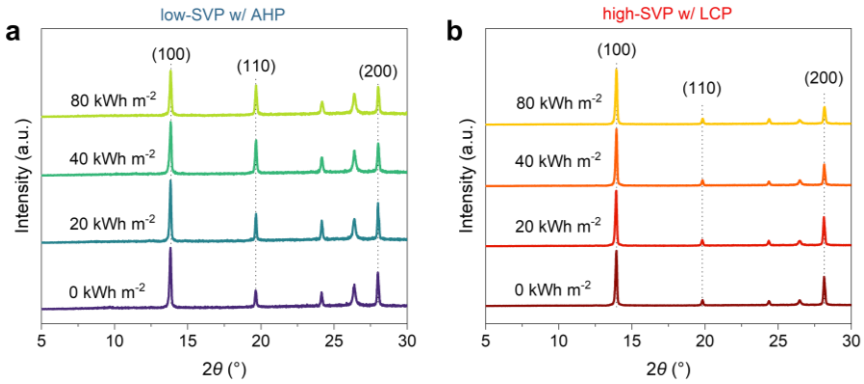

Supplementary Fig. 44 | XRD patterns of perovskite films after UV irradiation. a, The perovskite film prepared low-SVP solvent w/ AHP. **b,** The perovskite film prepared high-SVP solvent w/ LCP. No obvious degradation for both perovskite films under the UV aging. However, in the conventional low-SVP w/ AHP system, the perovskite film undergoes subtle changes in crystallographic orientation upon cumulative UV irradiation doses of 20, 40, and 80 kWh m^{-2}. Specifically, the diffraction intensity of the (100) plane decreases, while that of the (110) plane increases relatively. In contrast, no such shift is observed in the high-SVP system with LCP passivation.

2. The manuscript states that the commercial-scale perovskite modules are fabricated in ambient air. It is important to clarify the air-exposure tolerance of the two strategies

before subsequent back-end processing (e.g., C_{60} evaporation, ALD SnO_2 and electrode). Specifically, if the freshly deposited perovskite layers are deliberately aged in air for a defined period prior to continue the subsequent deposition, how significantly does this delay impact the final module performance? Quantifying this effect would be highly relevant for assessing the robustness and practical feasibility of the proposed fabrication routes in industrial settings.

Response: We sincerely thank the reviewer for raising this insightful and highly practical question. The point regarding the "air-exposure tolerance" of perovskite layers in an industrial setting is indeed critical. In response, we have conducted a comparison of the PCEs of perovskite solar modules before and after deliberate aging in ambient air, in order to quantitatively assess the impact of such exposure.

In Supplementary Fig. 41, we evaluated the microstructural evolution of different perovskite films and confirmed that the LCP-modified high-SVP perovskite possesses superior air tolerance. After exposure to ambient air at room temperature (30–50% relative humidity, RH) for 24 hours, the LCP-treated film retained its crystalline integrity, whereas the AHP-treated film underwent severe morphological degradation characterized by the formation of honeycomb-like pores due to moisture ingress. Correspondingly, the XRD patterns showed significantly enhanced diffraction peaks corresponding to PbI_2 in the AHP-modified sample (Supplementary Fig. 42).

Building on this, we re-fabricated the aged perovskite films (after different passivation treatments) into full modules to quantitatively assess the impact of air aging on device performance (followed by the sequential deposition of subsequent functional layers such as thermally evaporated C_{60} and ALD SnO_2, ultimately yielding complete modules). As shown in Supplementary Fig. 72, the PCE of the AHP-modified, low-SVP-derived device degraded by 12.71%, whereas that of the LCP-protected, high-SVP-based module decreased by only 1.35%.

We now revised manuscript and supplementary information as follows:

"*Indeed, upon exposing the perovskite films to ambient air at room temperature (30-50% relative humidity, RH) for 24 hours, the LCP-modified film maintained excellent crystalline integrity. In contrast, the AHP-modified film underwent severe morphological degradation, developing a honeycomb-like porous structure as a result of moisture infiltration (Supplementary Fig. 41), which accelerated the perovskite decomposition (Supplementary Fig. 42).*"

"*We first demonstrated that the LCP strategy fulfills the requirement for tolerance to air exposure during fabrication (Supplementary Fig. 72) and subsequently investigated the efficiency degradation and morphological evolution of PSMs*

fabricated with AHP and LCP under IEC-standard testing conditions."

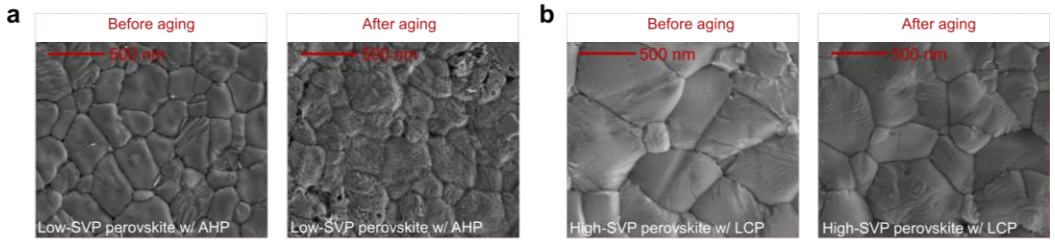

Supplementary Fig. 41 | Top-view SEM images of perovskite films after air aging (30%-50% RH, 24 h). a, Low-SVP perovskite with the corresponding AHP. **b,** High-SVP perovskite with the corresponding LCP.

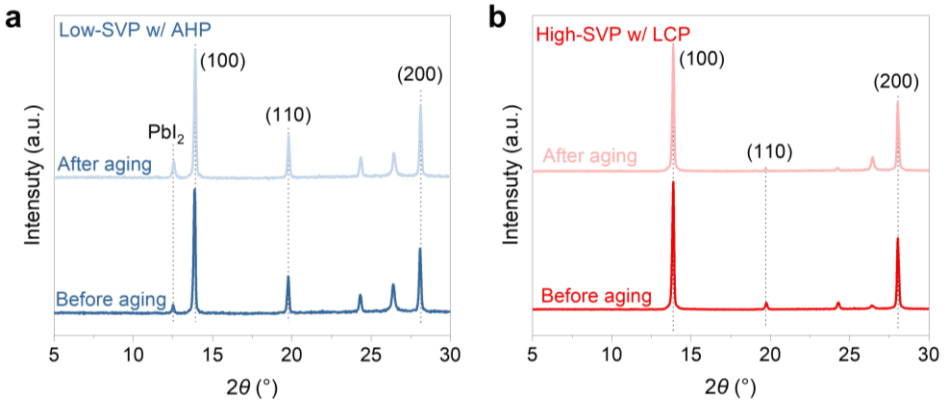

Supplementary Fig. 42 | XRD patterns of perovskite films after air aging (30%-50% RH, 24 h). a, Low-SVP perovskite with the corresponding AHP. **b,** High-SVP perovskite with the corresponding LCP.

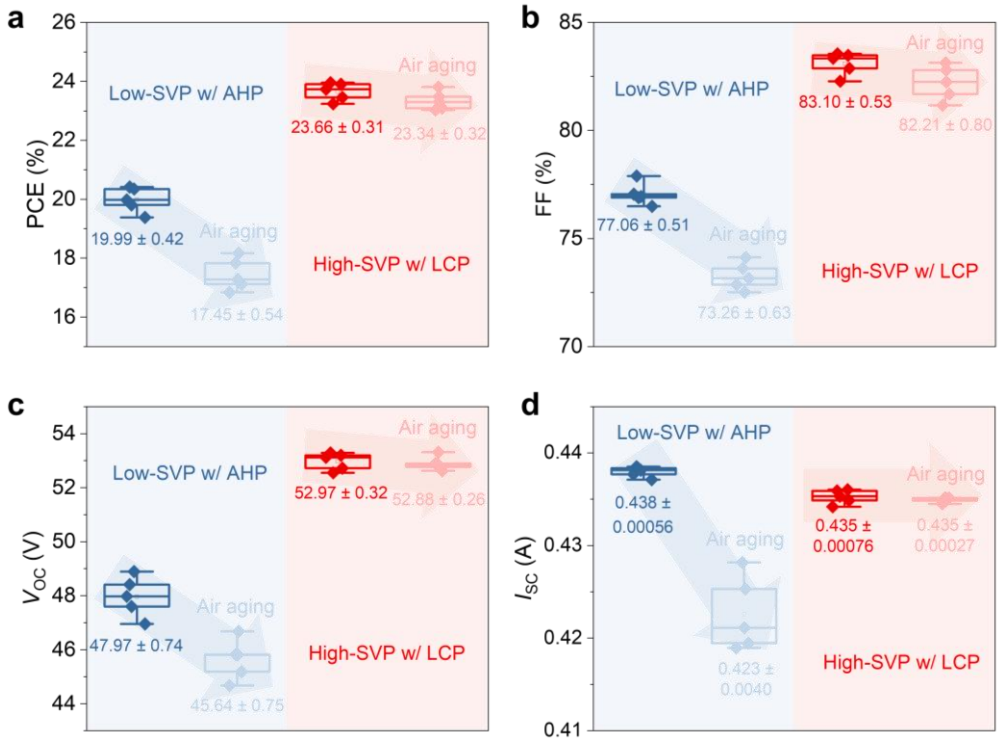

Supplementary Fig. 72 | Statistical photovoltaic parameters of the modules (Aperture area = 810 cm^2, 5 modules for each type). a, PCE, **b,** FF, **c,** V_{OC}, **and d,** I_{SC}. The aging conditions were identical to those described in Supplementary Fig. 41. Subsequently, the remaining functional layers were deposited sequentially, such as thermally evaporated C_{60} and ALD SnO_2, to complete the module fabrication. Scatters represent raw data; boxplots show the interquartile range with the median as the center line; whiskers indicate the 5th–95th percentiles. Numerical data are presented as mean ± SD.

3. The assertion in the paragraph titled "The formation of FAI-enriched surface…" that FAI is selectively carried to the top surface lacks sufficient theoretical justification and experimental evidence. Please provide a more detailed mechanistic explanation, supported by relevant data or references. Furthermore, the reasoning appears specific to FAI; please clarify why other constituent materials (e.g., PbI_2, Cs^+) do not exhibit similar surface-enrichment behavior under the same processing conditions.

Response: We sincerely appreciate the insightful and constructive comments. We have carried out additional experiments and theoretical analyses to address the issue of "FAI surface enrichment" and its specificity relative to other constituents. Specifically, we analyzed the distribution of Pb^+ and Cs^+ in the high SVP samples (Supplementary Fig. 12), performed XPS depth profiling to compare surface and bulk binding states (Fig. 1d and Supplementary Fig. 13), and conducted binding energy calculations for different solvents with FAI (Supplementary Fig. 15). Based on these results, we have proposed a surface model for the perovskite film with FAI-rich termination (Supplementary Fig. 14).

We now revised manuscript and supplementary information as follows:

"X-ray photoelectron spectroscopy (XPS) showed that the high-SVP perovskite surface exhibits binding energies (I 3d, N 1s) nearly identical to bare FAI, while its bulk characteristics resemble those of the low-SVP perovskite (Fig. 1d and Supplementary Fig. 13); this indicates that the FA^+ and I^- ions reside in an essentially uncoordinated state at the surface.

The formation of the FAI-enriched surface is attributed to the vacuum-induced directional migration of solvent from the film interior toward the upper surface, which drives convective transport and facilitates the accumulation of solute (FAI) on the wet perovskite film (Supplementary Fig. 14). This directional solvent flow entrains a high concentration of dissolved FAI toward the liquid-air interface, thereby inducing supersaturation and subsequent precipitation. Crucially, this directional co-transport is significantly enhanced by the strong hydrogen-bonding interactions between 2-Me

and FAI (Supplementary Fig. 15), providing a mechanistic rationale for the preferential surface enrichment."

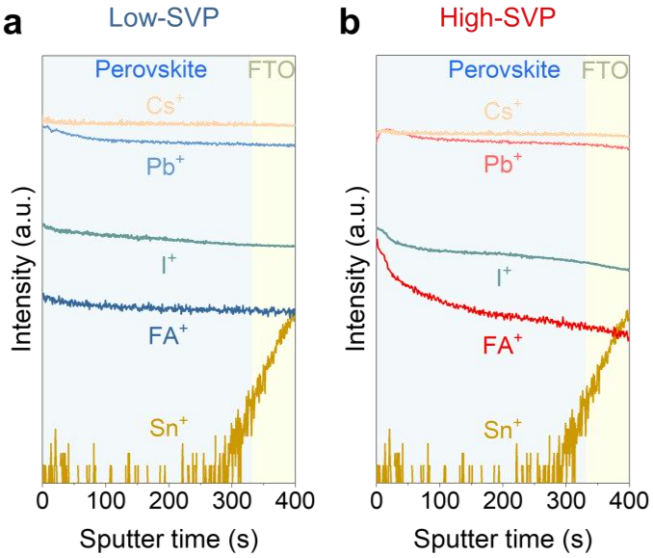

Supplementary Fig. 12 | TOF-SIMS depth profile of the perovskite films. a, Low-SVP perovskite, **b,** High-SVP perovskite.

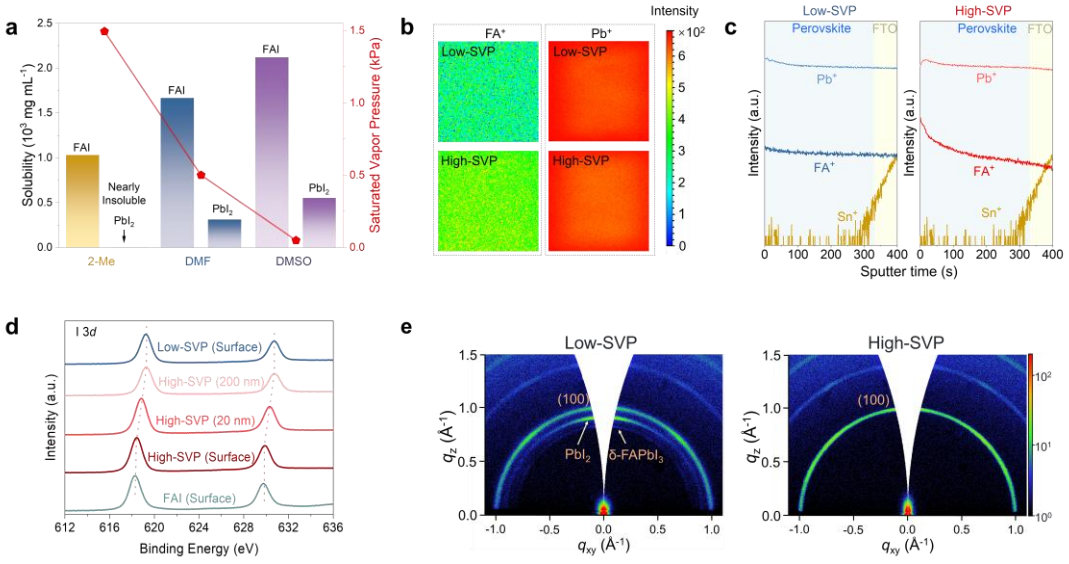

Fig. 1 | Surface states of perovskite films. a, Solubility of FAI and PbI_2 in 2-Me, DMF, and DMSO, and the saturated vapor pressure of these solvents at room temperature. **b,** TOF-SIMS surface ion mapping of the FA^+ and Pb^+ on the low-SVP and high-SVP prepared perovskite films. **c,** TOF-SIMS depth profile of the perovskite films. **d,** I 3*d* XPS spectra of pristine FAI, and perovskite films prepared from low-SVP and high-SVP solvent systems. **e,** GIWAXS patterns of the perovskite films prepared by low-SVP and high-SVP.

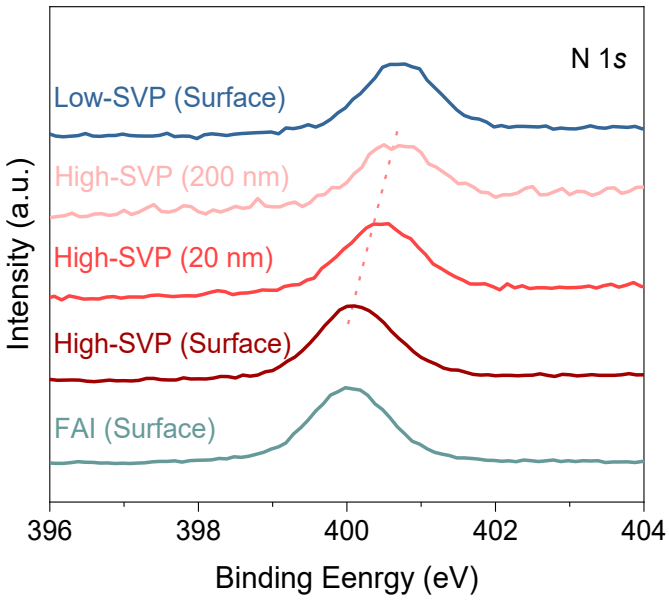

Supplementary Fig. 13 | XPS spectra. N 1*s* XPS spectra of FAI powder and perovskite films fabricated using low-SVP and high-SVP solvents. Measurements for FAI and the low-SVP perovskite were confined to the top surface, while those for the high-SVP perovskite included the top surface and depths of 20 nm and 200 nm.

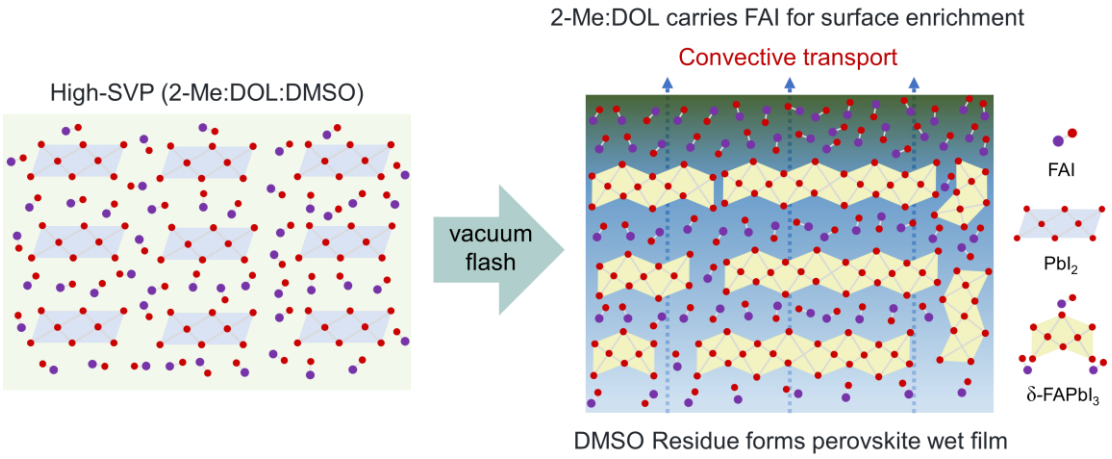

Supplementary Fig. 14 | The schematic illustration of the dynamic process of the surface enrichment of FAI during VCD processing. The high SVP characteristic of 2-Me induces its rapid evaporation under vacuum conditions. This establishes a steep concentration gradient and intense Marangoni flow, thereby driving the migration of FAI toward the liquid–air interface. Owing to the kinetic trapping effect during rapid solvent removal (where the solvent evaporation rate far exceeds the solute diffusion rate, causing FAI transported to the interface to be trapped by the rapidly forming solid perovskite matrix before redistributing into the bulk), FAI species are preferentially accumulated and stabilized at the perovskite surface, ultimately forming an FAI-enriched termination layer.

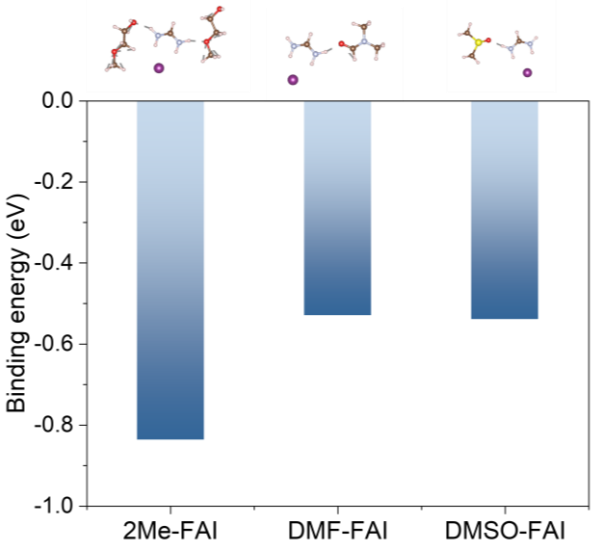

Supplementary Fig. 15 | Binding energy calculations of FAI and solvents. The 2-Me exhibits a higher binding energy with FAI compared to DMF or DMSO. This indicates a stronger interaction between 2-Me and FAI, suggesting that 2-Me forms more favorable associations with FAI species.

4. The novelty of the claim regarding high-SVP solvents enabling surface customization via VCD is unclear. Please provide references to support its originality or clarify how it differs from prior work.

Response: We sincerely thank the reviewer for highlighting the need to better contextualize the novelty of our high-SVP solvent-based VCD approach. In the following response, we have clarified the original contributions of this strategy by distinguishing it from prior solvent-engineering and VCD-related works, and have added relevant citations to support our discussion.

We acknowledge that the application of VCD to pre-crystallize perovskite films is a well-established approach, and solvent engineering has been used in combination with VCD to achieve larger-area, more uniform thin-film deposition (e.g., Science, 2025, 390, 1021-1028; Nature, 2025, 648, 91–96; Nature, 2024, 634, 1091–1095). In addition, a limited number of studies have reported spontaneous surface enrichment leading to in situ passivation. For example, Hu et al. demonstrated that adding S-benzyl-L-cysteine (SBLC) to the perovskite precursor results in the spontaneous formation of a SBLC-PbI_2 2D perovskite capping layer atop the 3D perovskite during drying, attributed to the limited solubility and amphiphilic nature of the SBLC adduct (Adv. Energy Mater., 2020, 10, 2000173).

However, prior work has largely treated two aspects independently: the influence of solvent SVP in VCD processes, and the interface enrichment induced by bulk additives during crystallization due to factors such as solubility, molecular size, or

specific physicochemical properties. A systematic linkage among the VCD process, the perovskite precursors (e.g., PbI_2, FAI, CsI), and the solvent system has not been well established.

The novelty of this work is primarily reflected in the following aspects:

- It revealed the relationship between the solvent evaporation kinetics under VCD technique and the microscopic distribution of perovskite components.
- It enables controllable fabrication of a perovskite surface passivation avoid using organic salts, achieving a moisture-resistant and stable perovskite film through the use of LCP.

We now revised the introduction section in manuscript as follows:

"*Although several solvent engineering strategies have been explored to regulate perovskite crystallization via the VCD technique, the interplay between evaporation kinetics and the resulting component distribution at the microscopic scale remains ambiguous.*"

"*Here, we reveal the relationship between the solvent evaporation kinetics under VCD and the microscopic distribution of perovskite components. Specifically, we design a formamidinium iodide (FAI)-enriched perovskite surface through a high-SVP solvent system, composed of 2-Me, 1,3-dioxolane (DOL), and DMSO, which then upon reaction with a LCP , lead dioleate ($Pb(OA)_2$), forms an atmospherically robust barrier.*"

5. Regarding Fig. 2b, the authors note a coffee-ring effect after AHP treatment. While the PL mapping indicates spatial inhomogeneity, additional experimental evidence (e.g., optical microscopy, or SEM surface imaging) would strengthen this observation. Furthermore, the underlying causes of this effect should be discussed.

Response: We thank the reviewer for the constructive suggestion. We have supplemented the optical microscopy and SEM surface images of the AHP-treated film (Supplementary Fig. 39), which demonstrates the coffee-ring-like morphological inhomogeneity. The Supplementary Note 4 provides a detailed discussion of the underlying causes of this phenomenon, attributing it to the significant differences in the dissolution state, diffusion coefficient (D), and Marangoni flow strength between AHP and LCP in IPA.

"***Supplementary Note 4:***

The coffee-ring effect of AHP in IPA solution.

We attribute the observed coffee-ring effect to a mismatch between solubility and diffusion rate. In IPA, AHP ($EDAI_2$) forms a typical coffee-ring deposit, while LCP

($Pb(OA)_2$) yields a uniform film. The underlying mechanism stems from fundamental differences in solute state, diffusion coefficient (D), and Marangoni flow intensity between the two systems in IPA. The coffee-ring effect arises during droplet drying when the contact line is pinned, preventing overall droplet contraction. To compensate for the rapid evaporation at the edge, a sustained outward capillary flow develops within the droplet. This flow transports solutes toward the periphery. When the rate at which solutes are carried to the edge exceeds their rate of return to the center via Brownian diffusion, solute accumulates at the edge, forming a ring-like deposit.

$Pb(OA)_2$ exists in IPA primarily as colloidal nanoparticles or large molecular clusters, with sizes ranging from several to tens of nanometers. Its large size results in a very low diffusion coefficient (D). Although the initial capillary flow carries particles toward the edge, their extremely low diffusivity causes rapid accumulation and the formation of a solid shell at the periphery, which triggers depinning of the contact line. The subsequent retraction of the contact line (in a "sliding" mode) interrupts the sustained outward capillary flow, a key factor in achieving uniform deposition. Moreover, $Pb(OA)_2$ acts as a surfactant, creating a pronounced concentration gradient at the liquid surface that induces strong Marangoni flow (driven by surface tension gradients). This internal convection effectively mixes the droplet, further suppressing ring-like solute segregation.

In contrast, $EDAI_2$ in IPA is a fully dissolved small-molecule ionic compound ($EDAI^+$ and I^-) with molecular-scale dimensions (<1 nm) and exhibits a very high diffusion coefficient (D) in the low-viscosity solvent. The high interfacial tension between IPA and the perovskite leads to strong pinning of the contact line, hindering its retraction, while continuous evaporation at the edge generates a robust, steady outward capillary flow. Under the rapid-drying conditions of slot-die coating or droplet evaporation (high evaporation flux J), the Péclet number ($Pe = JR/D$, where R is the characteristic length) is much greater than 1, indicating that convective transport far outpaces the return of molecules to the center via diffusion. Additionally, compared to $Pb(OA)_2$, $EDAI_2$ has a negligible effect on the surface tension of IPA, failing to generate a sufficiently strong counteracting Marangoni flow to offset the capillary flow.

In summary, the $Pb(OA)_2$/IPA system suppresses coffee-ring formation through the synergistic action of depinning induced by low diffusivity and strong Marangoni convection. Conversely, the $EDAI_2$/IPA system produces the characteristic coffee-ring deposit due to the combined effects of high diffusivity, strongly pinned contact line, capillary-flow dominance at high Pe, and weak Marangoni effects. This analysis provides a clear physical picture of how solvent-solute interactions govern the uniformity of printed films.

We performed microscopic SEM characterization of the coffee-ring effect induced by AHPs, as shown in Supplementary Fig. 39. In the PL mapping, regions with lower PL intensity appear darker. The corresponding SEM images reveal that these areas exhibit localized, flake-like aggregates, which obscure the perovskite grain boundaries and crystal facets. Notably, the prevalence of these flake-like aggregates diminishes as the PL brightness increases. Based on the theoretical analysis above, we propose that the coffee-ring effect drives the localized accumulation of AHPs, forming flake-like aggregates. Such high-concentration local stacking is detrimental to the photovoltaic performance of the modules."

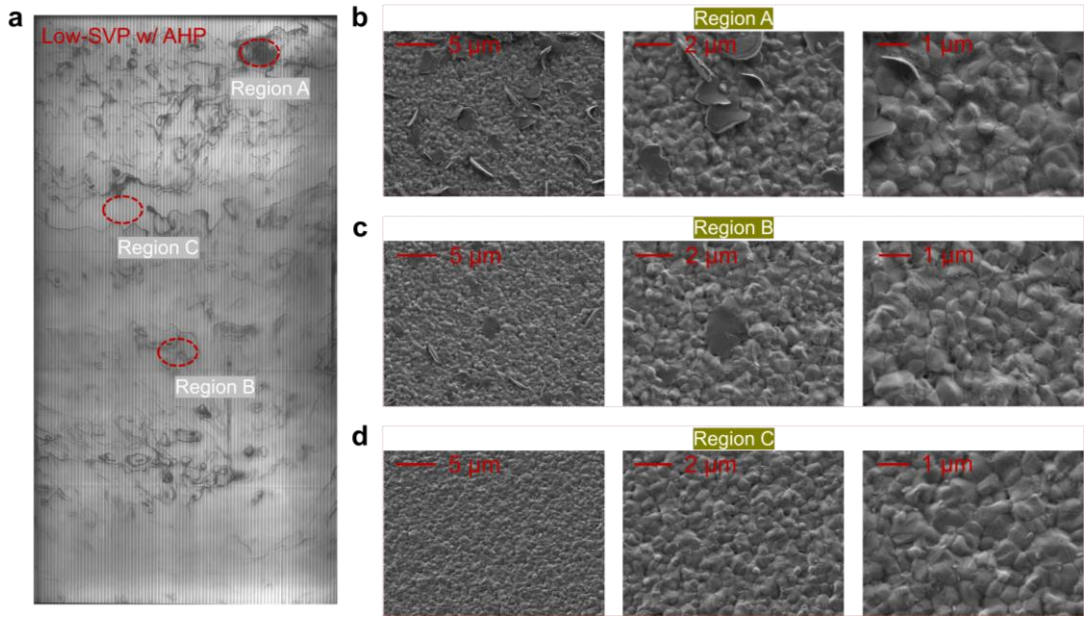

Supplementary Fig. 39 | Microscopic manifestation of the coffee-ring effect. a, PL mapping of AHP commercial-scale PV module. **b-d,** SEM images of the perovskite surface after AHP passivation, showing different regions. Region A, region B, and region C correspond to areas with increasing PL intensity (from dark to bright) in the PL mapping.

6. In the reliability section, providing the evolution of VOC, JSC, and FF before and after aging, rather than only normalized PCE, would offer deeper insight into whether the benefit of LCP mainly arises from reduced recombination, suppressed resistance buildup, or improved carrier collection.

Response: Thank you for the valuable suggestion. In the revised Source Data, we have supplemented the evolution of the individual photovoltaic parameters (V_{OC}, I_{SC}, and FF) before and after aging, in addition to the corresponding PCE (see Supplementary Figs. 73–75). In addition, we have included three months of outdoor power station data (Supplementary Fig. 89).

We now revised manuscript and supplementary information as follows:

"After 1,300 h of damp-heat testing (85% RH/85 °C, ISOS-D-3), AHP-based modules lost 39% of their initial efficiency (relative), whereas the LCP-modified modules exhibited only 2% relative loss (Fig. 5a, Supplementary Fig. 73). After 300 thermal cycling (between -40 °C and 85 °C, ISOS-T-3), the LCP-modified modules exhibited negligible efficiency loss (Fig. 5b, Supplementary Fig. 74). The LCP-modified modules retained 96% of their initial efficiency after 2,200 h under MPPT (Fig. 5c), and 95% of their initial performance under ultraviolet aging for a total solar irradiance of 30 kWh m^{-2} (Supplementary Fig. 75)."

"We conducted a three-month monitoring campaign (March to May 2026) on a 1 MW perovskite photovoltaic system and a 3.5 MW silicon (TOPCon) photovoltaic system, both installed within the same utility-scale power plant (Supplementary Fig. 89). A comparative analysis of the specific yield over the monitoring period confirmed that all systems delivered stable power output. However, the perovskite module consistently outperformed its silicon counterpart in terms of daily specific energy yield. The monthly specific yield gain ratios for March, April, and May were 3.42%, 3.79%, and 5.81%, respectively, demonstrating superior real-world performance (Supplementary Fig. 90). These results validate the commercial viability of perovskite photovoltaic technology."

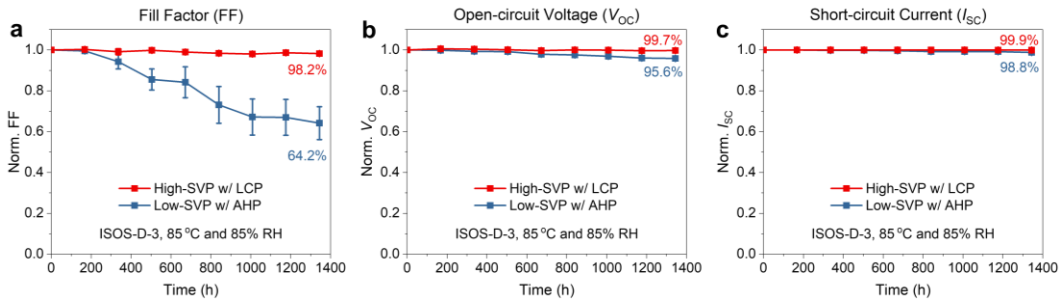

Supplementary Fig. 73 | Encapsulated PV modules aged under ISOS-D-3 testing protocol (5 modules for each type). Corresponding changes in the parameters **a,** FF, **b,** V_{OC}, and **c,** I_{SC}.

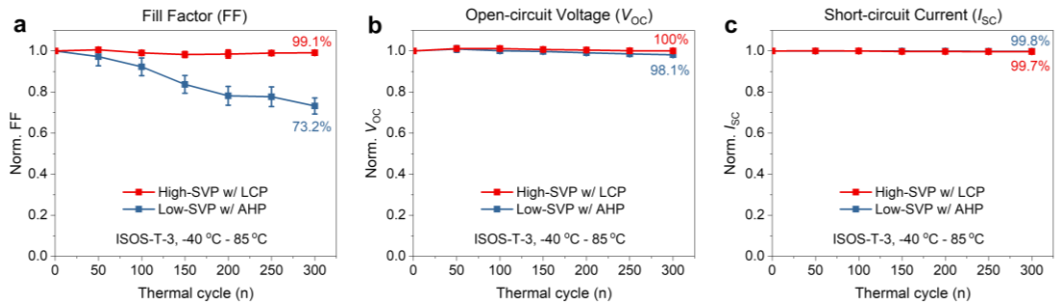

Supplementary Fig. 74 | Encapsulated PV modules aged under ISOS-T-3 testing

protocol (5 modules for each type). Corresponding changes in the parameters **a,** FF, **b,** V_{OC}, and **c,** I_{SC}.

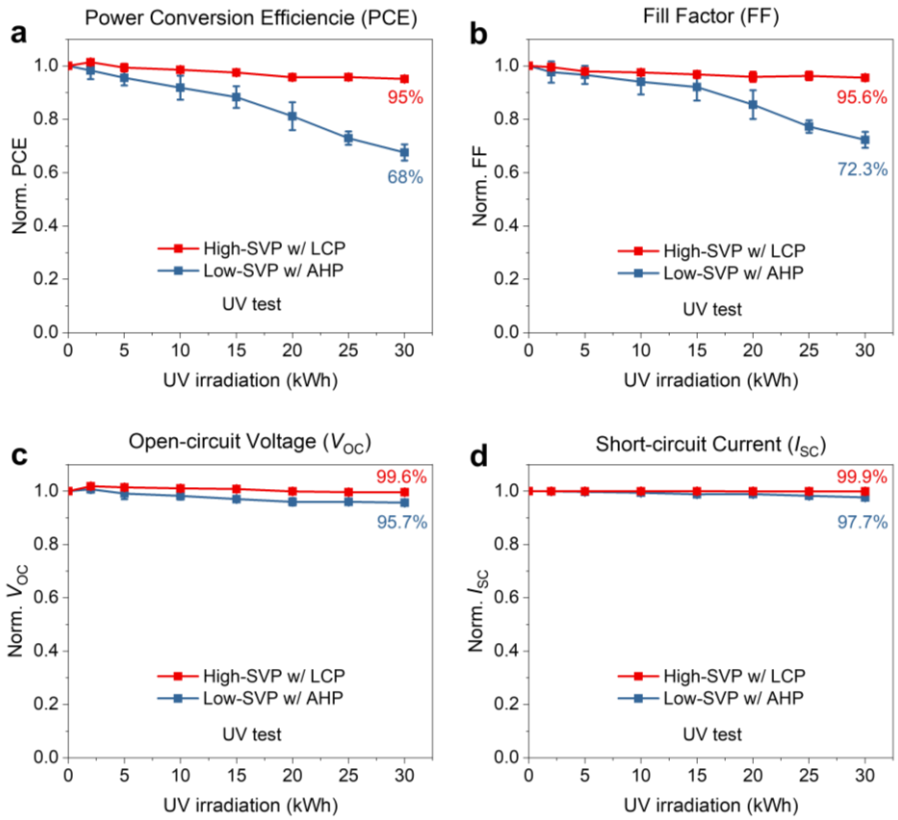

Supplementary Fig. 75 | UV preconditioning test with a cumulative UV irradiation of 36 kWh m^{-2} (5 modules for each type). Corresponding changes in the parameters **a,** PCE, **b,** FF, and **c,** V_{OC}, and **d,** I_{SC}.

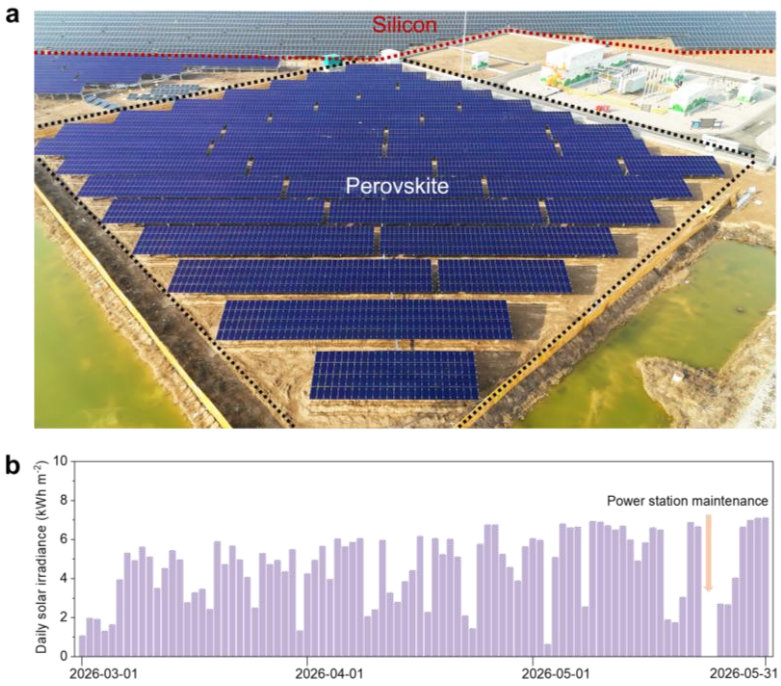

Supplementary Fig. 89 | Perovskite and silicon (TOPCon) photovoltaic power station. **a,** Photograph of the outdoor photovoltaic power station. **b,** Daily solar irradiance from March to May 2026.

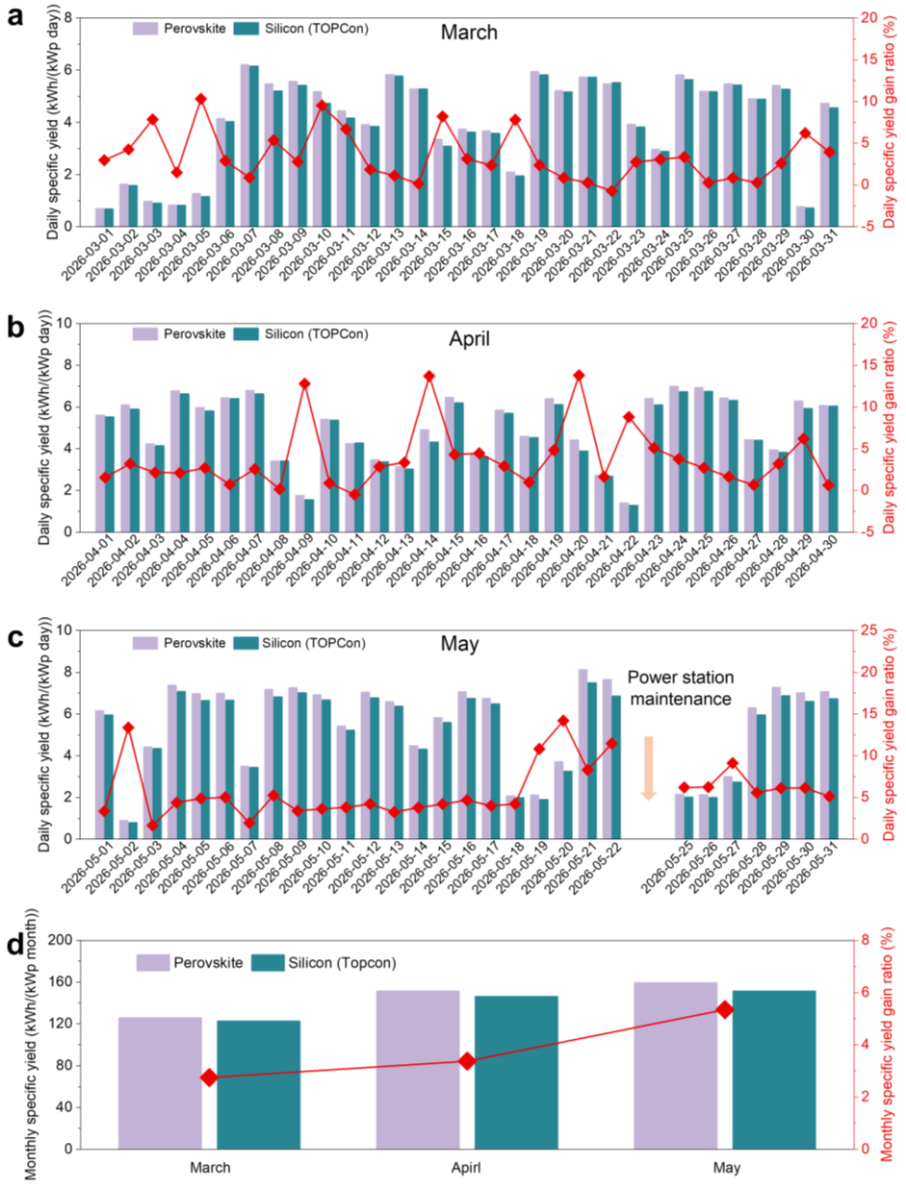

Supplementary Fig. 90 | Outdoor operational performance of perovskite and silicon PV station. a–c, Daily specific yield of the perovskite and silicon systems from March to May 2026. **d,** Monthly specific yield over the same period. The daily specific yield gain ratio represents the enhancement in daily specific energy yield of the perovskite relative to the silicon reference, calculated as (perovskite-silicon)/silicon.

7. The reported IEC 61215-related reliability results are impressive. A clearer summary table listing the conditions, endpoints, and evaluation criteria for each sub-test would improve readability.

Response: We thank the reviewer for the comment regarding the IEC 61215 reliability

test. We have listed the test sequences of the IEC 61215 and IEC 61730 standards in our previous work (Science, 2025, 390, 1021-1028), and we now also include them in Fig. R3, as shown below. In the revised Supplementary Information, we added a note that systematically lists the test conditions, pass/fail endpoints, and specific evaluation criteria for each sub-test, which enhances the readability and facilitates direct comparison.

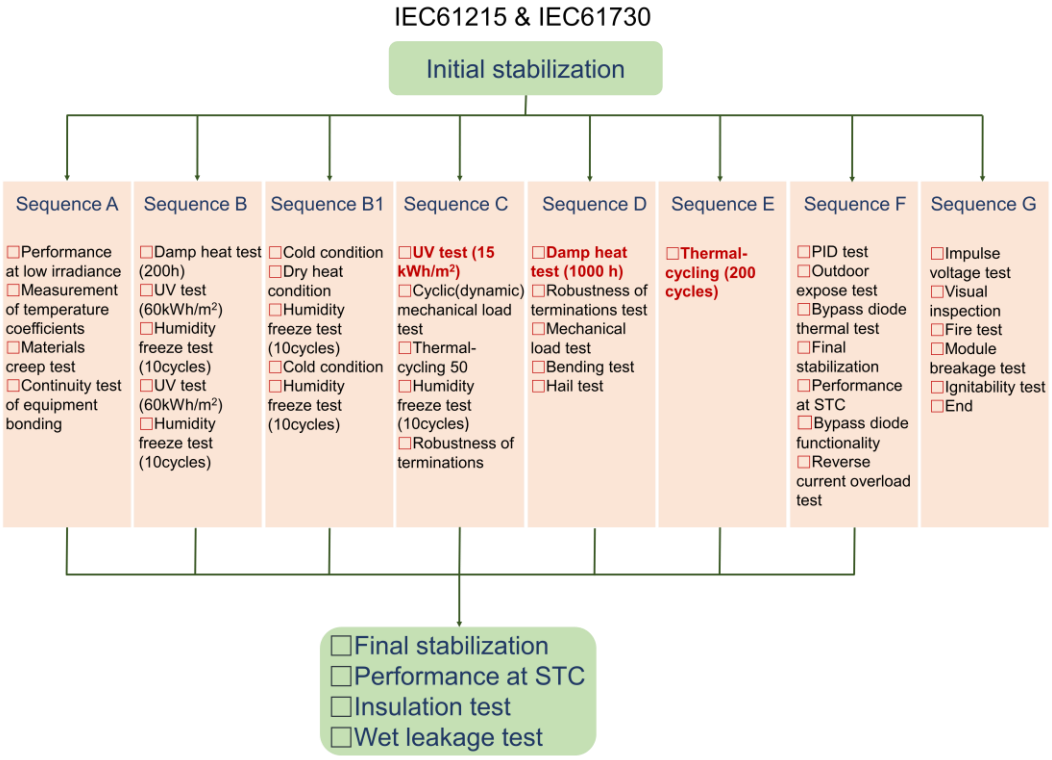

Fig. R3 | Items of the test sequences following IEC 61215 and IEC 61730 standards. The items marked in red were tested internally. (Science, 2025, 390, 1021-1028.)

"***Supplementary Note 6:***
The stability test in internal laboratory.

Purpose: Pre-treatment of components with UV radiation before thermal cycling/wet-freeze tests to evaluate materials and adhesives susceptible to UV aging.

Apparatus: a) Test chamber capable of maintaining component temperature at (60 ± 5) °C. b) Temperature sensor attached near the center of the component (front or back) without blocking light exposure. c) UV radiometer. d) UV light source with ±15% irradiance uniformity and capable of providing necessary total irradiance across different spectral ranges. e) Components can be short-circuited or open-circuited as per choice.

Procedure: a) Ensure wavelength range is 280 nm to 400 nm, with irradiance not exceeding 250 W/m^2 (5 times natural sunlight) and uniformity within ±15%. b) Install

components (short circuited or open-circuited) on the test plane, maintaining temperature at (60 ± 5) °C. c) Total irradiance must be at least 15 kWh/m^2, with component temperature maintained within the specified range.

Criteria: a) After 15 kWh of UV pre-treatment, power degradation should be ≤5%. Further testing may extend to 30–60 kWh, with power degradation ≤5%. The longer the duration, the better.

(ii) Damp Heat Test (1300 Hours)

Purpose: To evaluate the component's resistance to long-term humidity penetration.

Procedure: Conduct the test according to IEC 60068-2-78 and the following conditions: Temperature: (85 ± 2) °C; Relative Humidity: (85 ± 5)%; Duration: (1300 ±48) hours.

Final Testing: After recovery for 2-4 hours under open-circuit conditions at (23±5) °C and ≤75% relative humidity, repeat visual and wet leakage current tests. Power degradation after 1000 hours of aging should be <5%.
(iii) Thermal Cycling Test (300 Cycles)

Purpose: To measure the component's resistance to thermal mismatch, fatigue, and other stresses caused by temperature variations.

Apparatus: a) Fixtures to secure components in the environmental chamber, allowing free airflow. b) Temperature measurement tools with ± 2.0 °C accuracy and ± 0.5 °C repeatability. c) Continuous current supply device. d) Monitoring equipment for current flow during the test. e) Apply a 5 N weight to the junction box during testing.

Procedure: Heating/cooling rate: ≤1.7 °C/min. Cycle between -40 °C and +85 °C for 300 cycles. Hold at peak temperatures for at least 10 minutes. Apply Imp current during heating from -40 °C to +80 °C; otherwise, apply <1% Imp current.

Monitoring: Ensure junction box adhesion to the back sheet is maintained during testing. Apply a 5 N weight to the junction box during the test."

8. It would be useful to briefly comment on the main source of efficiency loss when scaling from 810 cm^2 to 0.72 m^2, for example in terms of geometric fill factor, interconnection loss, or large-area uniformity.

Response: We thank the reviewer for this insightful suggestion. Although the fabrication processes between 810-cm^2 and 0.72-m^2 modules are the same, the primary efficiency loss when scaling from the 810 cm^2 module to the full-size 0.72 m^2 module stems from three interrelated factors, listed in order of estimated contribution:

Patterning Losses: The 810 cm^2 and 0.72 m^2 modules mentioned in the text refer to the aperture area and the total area, respectively. For the total-area module, even without considering the interconnection losses (P1, P2, and P3), there is an inherent edge dead-area loss due to the design. As illustrated in Fig. R4, the perovskite active region lies within the red dashed boundary, accounting for 94.3% of the total module area. Consequently, based on the certified total-area efficiency of 22.0% for the 0.72 m^2 module, the corresponding active-area efficiency is calculated to be 23.3%. This value aligns closely with the certified efficiency of 24.0% for the 810 cm^2 (aperture area) module, indicating that the primary efficiency difference between the two formats can be attributed to geometric scaling losses.

Large-Area Coating Uniformity: As the module size increases, the impact of uniformity on device performance becomes more significant. However, with proper optimization, the uniformity quality can approach that of small-area devices. This can lead to localized regions with slightly different optoelectronic properties (e.g., bandgap, defect density), which manifests as a marginal reduction in the average V_{OC} and FF at the module level compared to the best small-area cells.

Series Resistance Increase: The longer, narrower cell stripes and the correspondingly longer busbars/tabs in the larger module contribute to an increase in the overall series resistance (Rs), which primarily impacts the FF. While carefully designed, this resistive loss becomes more pronounced at the module scale.

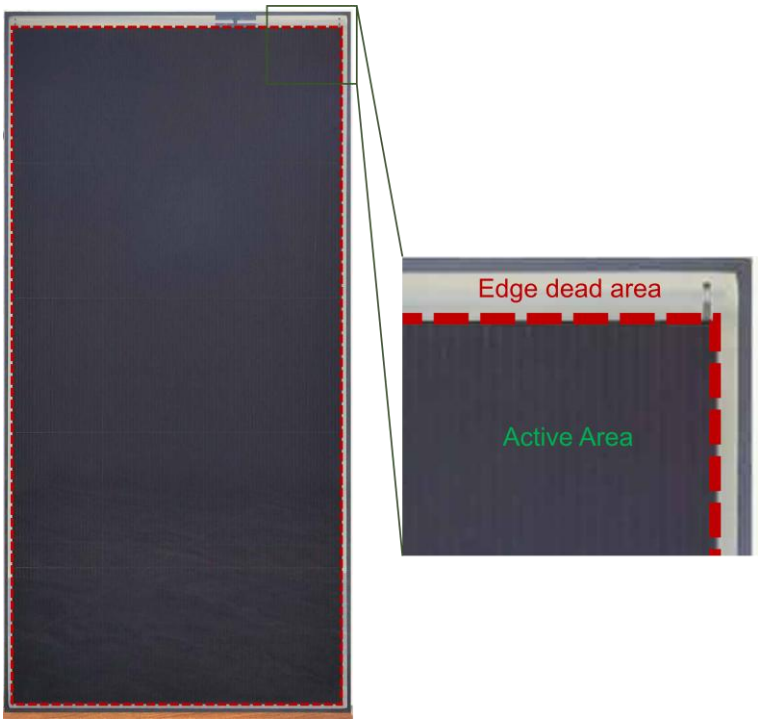

Fig. R4 | Image of the module (1.2 by 0.6 m^2). The region within the red dashed border

corresponds to the active perovskite area, while the surrounding region exhibits a distinct edge dead area. (Science, 2025, 390, 1021-1028.)

9. The authors should add a conclusion section that clearly discusses the industrial feasibility of this method. Additionally, future perspectives on the design of more robust and versatile passivation strategies for perovskite solar cells should be provided. This addition would significantly strengthen the paper's completeness and practical relevance.

Response: We appreciate the suggestion to strengthen the industrial feasibility and future outlook of this work. These additions substantially strengthen the manuscript's completeness and practical relevance. A discussion of these points has been integrated into the revised manuscript:

"*By integrating a high-SVP solvent system with a chemically stable LCP, we demonstrate a robust, industry-ready protocol for fabricating large-area perovskite modules at the meter scale. Crucially, this strategy not only achieves state-of-the-art performance but also passes the full suite of IEC 61215 qualification tests. Our findings establish a new benchmark for manufacturable perovskite photovoltaics, where processability, durability, and efficiency are no longer mutually exclusive but are engineered from the outset. This work thus charts a clear course toward the industrialization of perovskite solar technology.*"

Referee #3 (Remarks to the Author):

General Remarks

Xu et al. report perovskite modules with high efficiency and durability by fabricating FACs-based perovskite films with an FAI-rich surface via a vacuum chamber drying (VCD) process using a solvent combination with high saturation vapor pressure (HSVP), and subsequently passivating this surface with $Pb(OA)_2$. The buried interface was treated in the same manner as in conventional approaches using MeO-4PACz, while for the top surface, instead of using alkyl ammonium halides (AHP, including RP and DJ types) to compensate for A-site deficiency, the authors treated the FAI-rich surface with $Pb(OA)_2$. This appears to be a reasonable approach, and the role of this strategy seems to have been relatively well elucidated through model experiments.
From the perspective of commercialization of perovskite solar modules, this work appears to be part of the continuum of solvent formulation development for large-area processing using slot-die coating. In particular, the study is evaluated as providing a meaningful research direction for the community by proposing a surface passivation strategy that can overcome the durability issues associated with conventional AHP-based surface treatments. Therefore, the manuscript could be considered for publication if the following comments are adequately addressed.

Response: We sincerely thank the reviewer for the supportive and insightful summary of our work, and for recognizing its significance in the context of large-area processing and surface passivation research. We have carefully addressed the comments below and believe these revisions have further strengthened the clarity and impact of the study.

Detailed Comments

1. For the VCD process, the authors selected an HSVP solvent combination of 2-Me, DOL, and DMSO, and the role of DOL in securing the shelf life of the perovskite ink appears to have been well investigated. However, while the solvent properties of 2-Me and DMSO are presented, it seems necessary to also provide the solvent properties of DOL, including vapor pressure and solubility.

Response: We appreciate the reviewer's comment about the comprehensive description of the solvent properties. In response, we have provided the complete physicochemical characterization of DOL, 2-Me, DMF, and DMSO in the Supplementary Information, and these data have been incorporated into the revised Supplementary Table 1.

"***Supplementary Table 1***. *Physicochemical properties of DOL, 2-Me, DMF, and DMSO,*

*and their solubility for FAI and PbI_2. **Note.** Solubility measurements were conducted at room temperature. Values were determined by differential weighing after dissolving solutes into a supersaturated state. Minor errors may arise from this gravimetric approach.*"

		DOL	2-Me	DMF	DMSO
Boiling Point (°C)		75	128	153	189
SVP (kPa)		15.3	1.50	0.50	0.08
Solubility (mg mL^{-1})	**FAI**	Nearly insoluble	1030	1670	2130
	PbI_2	Insoluble	Nearly insoluble	310	550

2. From the perspective of large-area thin-film processing, studies on FACs-based perovskite inks using solvent combinations such as 2-Me, DMSO, or NMP have already been reported in the literature. In this work, the key differentiation appears to lie in the use of DOL. The role of DOL seems similar to that of 2-Me–THF previously reported by the same group. Therefore, it would be helpful if the authors comment on the specific reason for selecting DOL in this study and what limitations may arise when using 2-Me–THF.

Response: We appreciate the insightful comment regarding the selection of DOL in our high-SVP solvent system and the comparison with the previously reported 2-MeTHF system (Science, 2025, 390, 1021-1028).

In this work, we selected the 2-Me:DMSO solvent system as the solvent foundation. We found that when 2-Me (a high-SVP solvent) served as the primary solvent, it was well-compatible with the VCD process and enabled the fabrication of high-performance perovskite modules. However, the 2-Me:DMSO system alone could not adequately stabilize the perovskite ink. Therefore, we introduced DOL to stabilize the ink for production. Meanwhile, the formation of the FAI-enriched surface layer depends on the interaction between FAI and 2-Me, making the presence of 2-Me essential for achieving a gradient distribution of FAI. In previous report, the solvent system for perovskite inks consisted of a ternary mixture of 2-MeTHF, GVL, and DMSO, in which both GVL and DMSO are low-SVP solvents with high solubility for perovskite powders. The appropriate incorporation of 2-MeTHF (within a volume ratio of 50%)

did not pose solubility issues. However, our experimental results indicate that 2-MeTHF cannot play an effective role within the 2-Me:DMSO solvent system.

Now the relevant discussion is provided in the revised supplementary note 1:

*"**Supplementary Note 1:***

The cosolvency of DOL:2-Me mixed solvents

…2-Methyltetrahydrofuran (2-MeTHF), employed in perovskite ink formulation, shares similar molecular structure and saturated vapor pressure with DOL. However, replacing DOL with 2-MeTHF in the ternary solvent system (2-Me:2-MeTHF:DMSO) fails to effectively dissolve the perovskite precursors, as evidenced by persistent ink turbidity (Supplementary Fig. 11). This result further highlights the unique advantage of DOL in stabilizing the precursor solution."

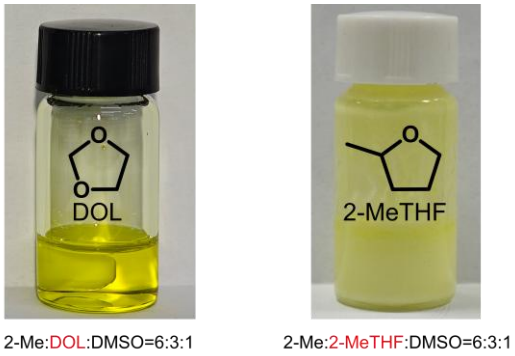

Supplementary Fig. 11 | The digital photos of the perovskite inks. DOL acts as a co-solvent to enhance solubility, whereas the ink remains turbid even after adding 2-MeTHF to the 2-Me:DMSO mixed solution.

3. In general, since the solubility of FAI in solvents used for dissolving perovskites is much higher than that of PbI_2, it is thermodynamically expected that a PbI_2-rich surface forms. To address this, it is commonly known that a slight excess of A-site precursors is added during perovskite film fabrication. In this context, it seems possible that an FAI-rich perovskite film could also be obtained by initially introducing excess A-site (FAI) in this work. Therefore, it would be beneficial to examine what happens when excess FAI is used.

Response: We appreciate the insightful comment regarding the thermodynamics of perovskite crystallization and the feasibility of obtaining an FAI-rich perovskite film via excess A-site precursor addition. We agree that, based on solubility differences, a PbI_2-rich surface is thermodynamically favored, and the conventional strategy involves adding a slight excess of A-site precursors to compensate for this. Our experimental results demonstrate that introducing excess FAI into the low-SVP solvent system

adversely affects the crystallinity, phase stability of the active perovskite phase, and the optoelectronic performance of the resulting modules. These findings further highlight the distinct advantages of employing the LCP strategy within the high-SVP solvent framework.

We have revised the manuscript and added a detailed discussion in the supplementary information:

"*Furthermore, introducing excess FAI into the low-SVP system fails to replicate the performance exhibited by the high-SVP approach (Supplementary Note 3, Supplementary Figs. 28–32), further suggesting the necessity and superiority of the proposed LCP method.*"

"***Supplementary Note 3:***

The performance of excess FAI in the low-SVP perovskite system.

To clarify that simply increasing the FAI content in the precursor is not a viable route for achieving high-performance modules, and to further highlight the necessity and superiority of our proposed method, we prepared low-SVP perovskite inks with 2%, 4%, and 6% excess FAI (molar ratio). Microscopically, excess FAI leads to larger and denser perovskite grains (Supplementary Fig. 28). However, XRD characterization reveals that excess FAI alters the crystallization orientation, exhibiting a progressively stronger (110) preferred orientation as the FAI content increases. Moreover, at 6% excess, the formation of the photo-inactive δ-$FAPbI_3$ phase is observed (Supplementary Fig. 29), which is detrimental to device performance. Consequently, we fabricated perovskite modules (810 cm^2) based on these compositions (Supplementary Fig. 30). A clear trend of declining efficiency is observed with increasing FAI excess, primarily manifested as a reduction in V_{OC} and FF, a result consistent with the XRD findings.

The perovskite module production line operates under ambient conditions with 30–40% RH. As outlined in Supplementary Note 2, the process from film coating to encapsulation and testing for a single module can be completed within a short timeframe, during which the perovskite film is exposed to air for a limited duration (typically <2 h). Owing to the low ambient humidity, brief exposure, and the protective effect of consecutively deposited functional layers (C_{60}, ALD-SnO_2, IZO, Cu), we observed no visible phase degradation of the perovskite films during the production process. However, when different perovskite films were placed in a flowing air environment with 60–70% RH, distinct stability variations emerged within just 1 h (Supplementary Fig. 31). Specifically, the low-SVP and 2% excess FAI perovskite films showed no significant visual change, whereas films with 4% and 6% excess FAI exhibited pronounced phase degradation. The degree of phase instability increased

with higher FAI content. XRD results confirm that this degradation process involves the facile transformation of excess-FAI perovskite films from the photoactive α-$FAPbI_3$ phase to the non-photovoltaic-active δ-$FAPbI_3$ phase under humid conditions.

In summary, merely introducing excess FAI is insufficient to achieve high-performance perovskite modules. Furthermore, its inherent instability under ambient conditions severely restricts the viability of this approach for large-scale atmospheric-environment manufacturing."

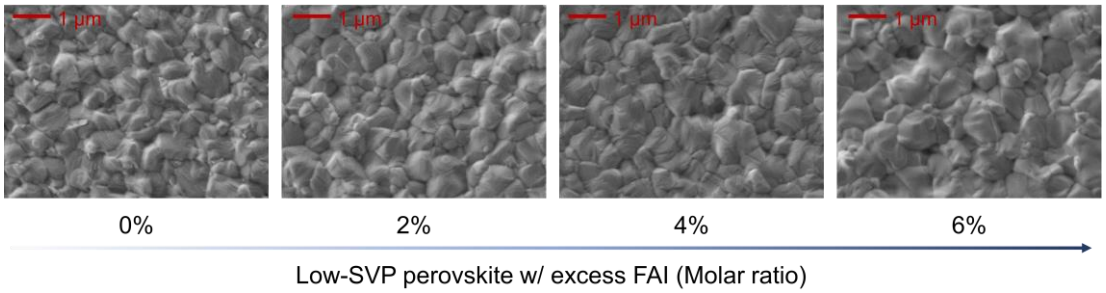

Supplementary Fig. 28 | Top-view SEM images of perovskite films. Perovskite film surfaces with varying excess FAI content.

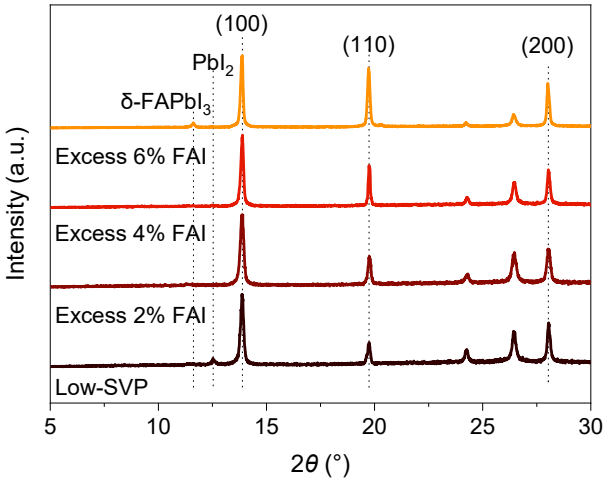

Supplementary Fig. 29 | XRD patterns of perovskite films. XRD patterns of the freshly prepared perovskite films, as shown in Supplementary Fig. 28.

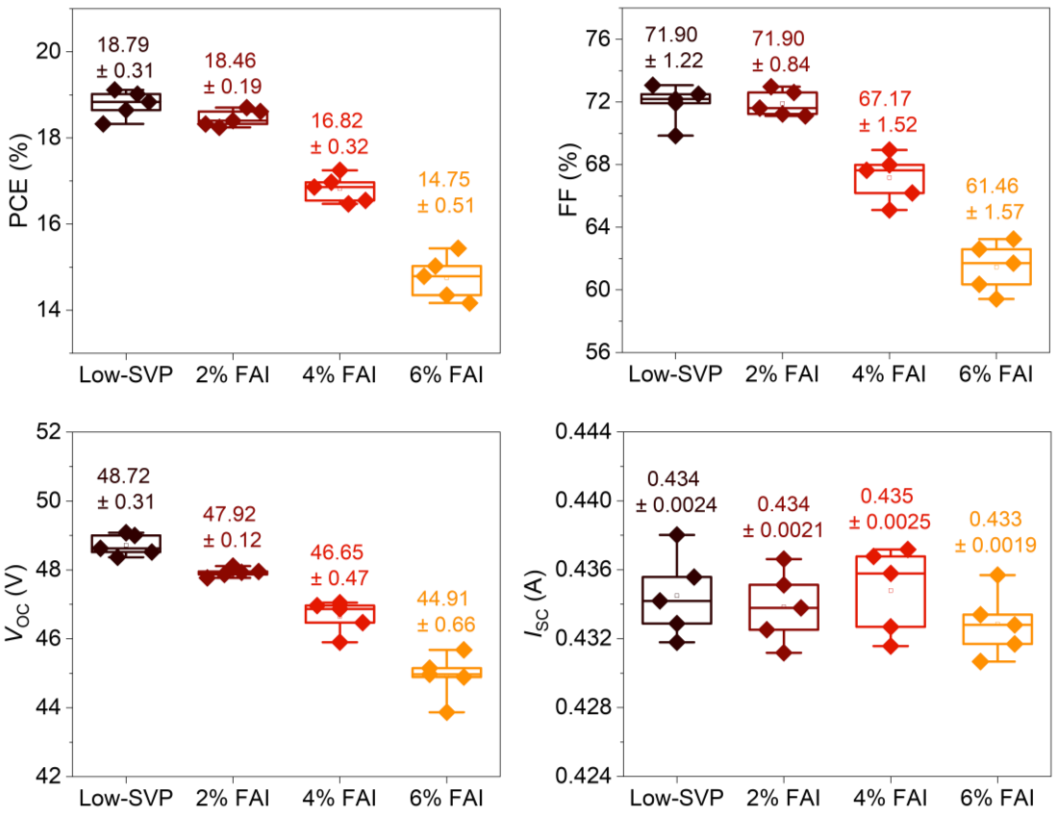

Supplementary Fig. 30 | Statistical photovoltaic parameters of the modules. The PV modules fabricated by low-SVP perovskite films with excess FAI. The aperture area of the module is 810 cm^2. Five parallel data sets were taken for each set of conditions. Scatters represent raw data; boxplots show the interquartile range with the median as the center line; whiskers indicate the 5th–95th percentiles. Numerical data are presented as mean ± SD.

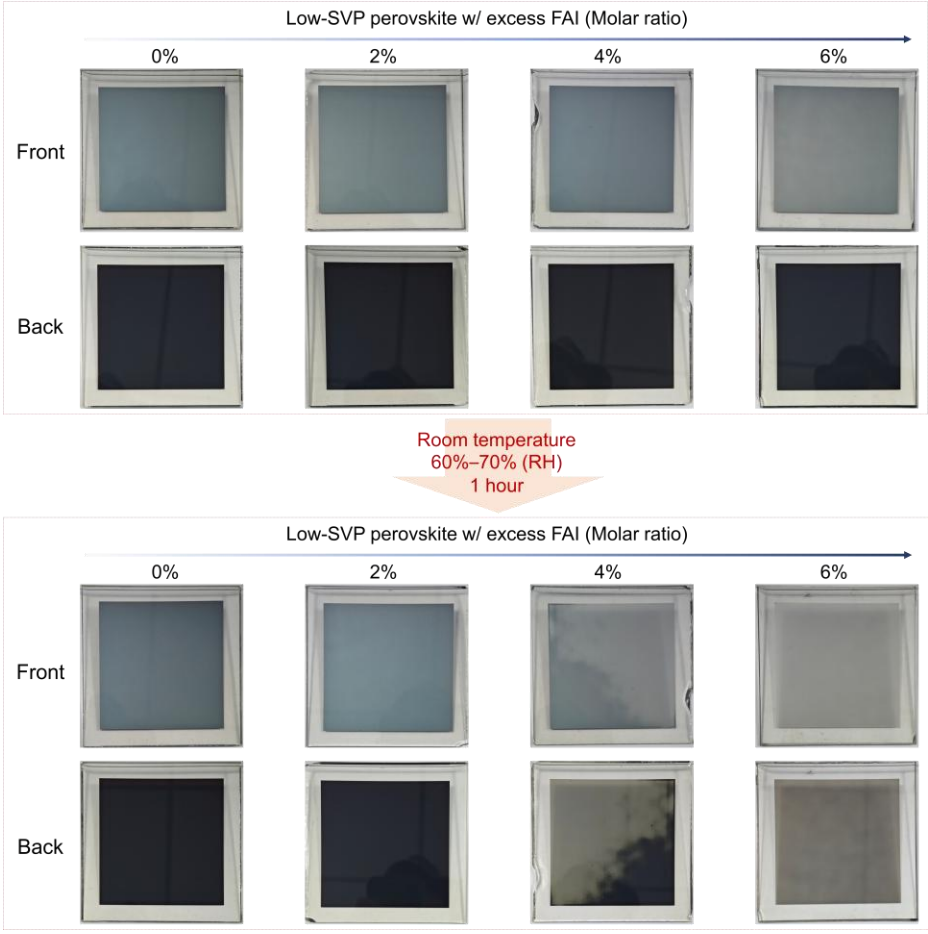

Supplementary Fig. 31 | Photographs of perovskite films before and after aging. Demonstrating the moisture stability of films with 0%, 2%, 4%, and 6% excess FAI (molar ratio) after exposure to 60–70% RH for 1 h.

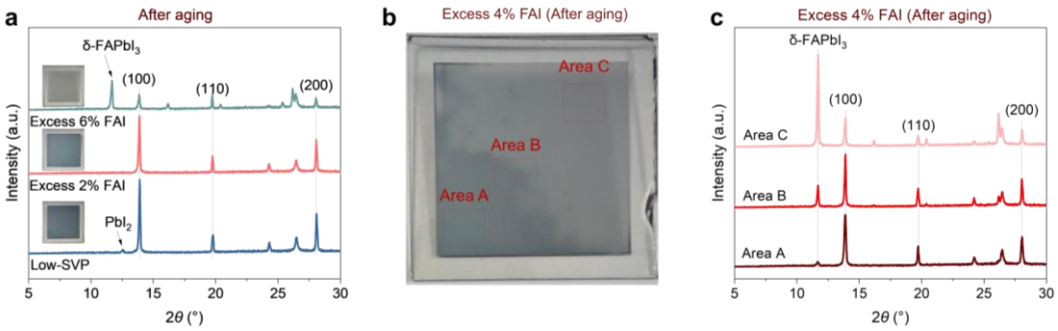

Supplementary Fig. 32 | The XRD patterns of perovskite films after aging (conditions shown in Supplementary Fig 31). a, XRD patterns of low-SVP films with 0%, 2%, and 6% excess FAI after aging. **b,** Photograph of the aged perovskite film with 4% excess FAI, divided into three regions exhibiting different degrees of decomposition (Area A, B, and C). **c,** Corresponding XRD patterns of the distinct regions (A, B, C) from the aged film with 4% excess FAI, as defined in panel b.

4. In the current manuscript, only two cases are compared: $Pb(OA)_2$ treatment on perovskite films prepared using HSVP solvents, and AHP treatment on films prepared

using LSVP solvents. It would be helpful to examine what happens when AHP is applied to perovskite films prepared using HSVP solvents.

Response: We appreciate the insightful suggestion to further clarify the specificity of the passivation strategy. In the original manuscript, the relevant experiments and discussions have already been conducted, as shown in Supplementary Fig. 45.

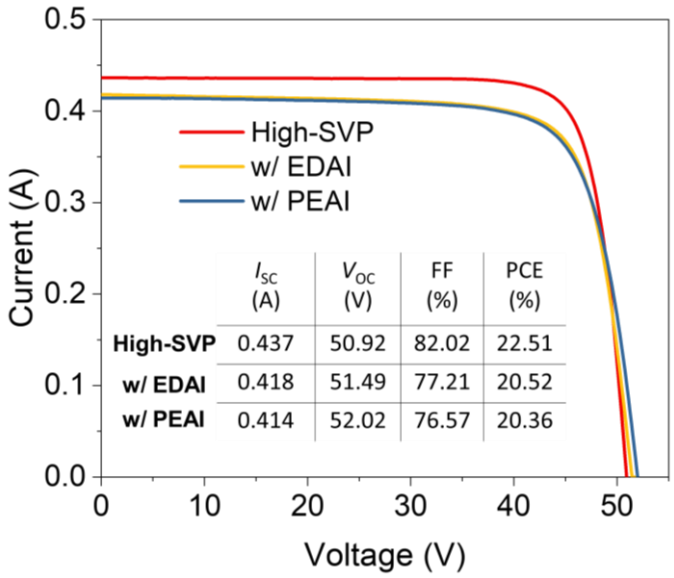

	I_{SC} (A)	V_{OC} (V)	FF (%)	PCE (%)
High-SVP	0.437	50.92	82.02	22.51
w/ EDAI	0.418	51.49	77.21	20.52
w/ PEAI	0.414	52.02	76.57	20.36

Supplementary Fig. 45 | *I-V* curves of perovskite modules. The modules made from high-SVP system with organic salt surface passivation.

5. In this study, $EDAI_2$ is used as an example of AHP. However, based on previous reports from the same group, AHPs such as TAC are expected to produce surfaces with hydrophobicity comparable to that of $Pb(OA)_2$. Therefore, it would be more appropriate to compare $Pb(OA)_2$ with AHP systems that exhibit similar hydrophobicity in order to better demonstrate the advantages of $Pb(OA)_2$.

Response: We thank the insightful comment. We acknowledge that TAC, as previously reported by our group, possesses a hydrophobic structure comparable to that of $Pb(OA)_2$. Therefore, comparing $Pb(OA)_2$ with AHP systems sharing a similar structural motif would provide a more rigorous and persuasive evaluation. We have added a detailed discussion and the corresponding experimental data in the revised manuscript and supplementary information:

"*We further evaluated the PCEs and reliability of AHP systems exhibiting hydrophobicity comparable to that of LCP (Supplementary Note 8, Supplementary Figs. 83–88), thereby validating the advantages of the LCP strategy.*"

"***Supplementary Note 8:***

The performance of modules modified hydrophobic AHP

We expanded the scope of AHP to include structures with hydrophobicity comparable to that of $Pb(OA)_2$. Specifically, we incorporated two distinct ammonium salts: trimethyltetradecylammonium chloride (TAC) and oleylamine hydrochloride (OAC) (Supplementary Fig. 83). By evaluating their performance within the low-SVP perovskite system, we provide a comprehensive validation of the advantages inherent to the LCP strategy.

Coating the perovskite surface with TAC and OAC yields hydrophobicity comparable to that of $Pb(OA)_2$ (Supplementary Fig. 84). Top-view SEM images reveal that both TAC and OAC treatments increase the surface roughness, yet induce distinctly different micro-morphologies (Supplementary Fig. 85). Upon introducing 1 mg mL^{-1} TAC, the surface develops a "fluffy" like texture with blurred grains, and increasing the concentration to 2 mg mL^{-1} further accentuates this disordered accumulation, resulting in a rougher film surface. In contrast, the OAC-treated perovskite exhibits polygonal grains of varying sizes, accompanied by well-defined and effectively filled grain boundaries, leading to a highly compact film. XRD characterization demonstrates that TAC removes surface PbI_2 but fails to form a two-dimensional (2D) structure, whereas OAC not only eliminates PbI_2 but also generates a low-dimensional perovskite phase (Supplementary Fig. 86). Consequently, we propose that TAC molecules tend to aggregate at the perovskite surface or grain boundaries, potentially increasing the interfacial resistance and impeding efficient carrier transport. In contrast, the long alkyl chains of OAC induce the formation of a 2D perovskite layer at the surface, which eliminates surface PbI_2 and promotes the growth of smaller perovskite crystallites.

Based on this, we fabricated perovskite modules with an active area of 810 cm^2. Both TAC and OAC modifications yielded a marginal increase in module efficiency (Supplementary Fig. 87). Subsequent stability testing of the modified modules revealed performance degradation under various conditions (Supplementary Fig. 88). Specifically, under ISOS-D-3 damp-heat testing, both module types degraded by approximately 10% within 500 h. Under ISOS-T-3 thermal cycling, efficiencies were maintained at only about 90% of the initial value after 150 cycles. Similarly, under UV aging, the modules exhibited a 10% efficiency loss after 14 kWh of cumulative irradiation. All these data demonstrate that the stability performance of the TAC and OAC modified modules is inferior to that achieved with the LCP strategy, further highlighting the superior performance provided by LCP passivation."

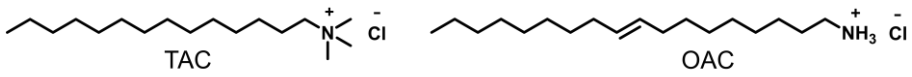

Supplementary Fig. 83 | Molecular Structures of TAC and OAC.

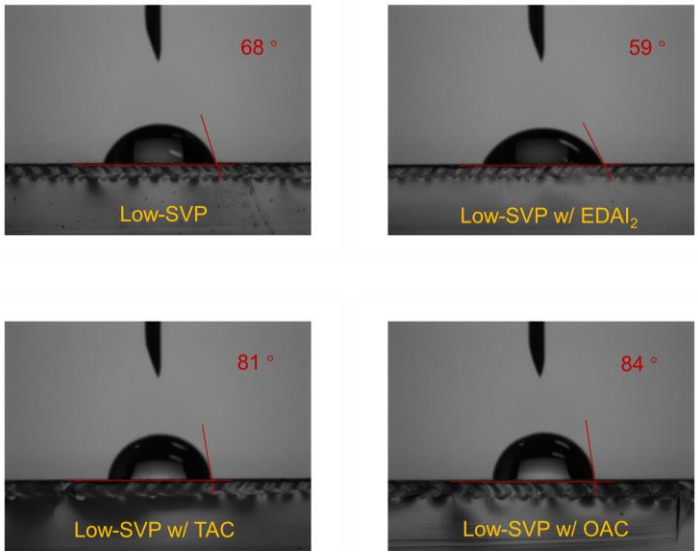

Supplementary Fig. 84 | Water contact angle measurements on perovskite film surface. The perovskite surfaces were modified with $EDAI_2$, TAC, and OAC, respectively.

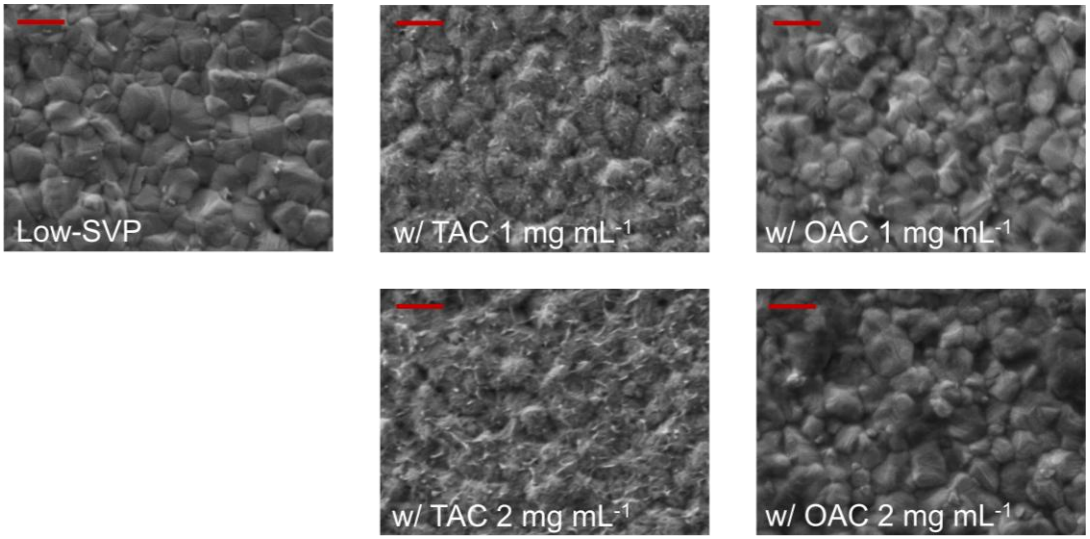

Supplementary Fig. 85 | SEM images of low-SVP perovskite films. The top-view SEM images of low-SVP perovskite film with TAC and OAC passivation. The scale bars correspond to 1 μm in all images.

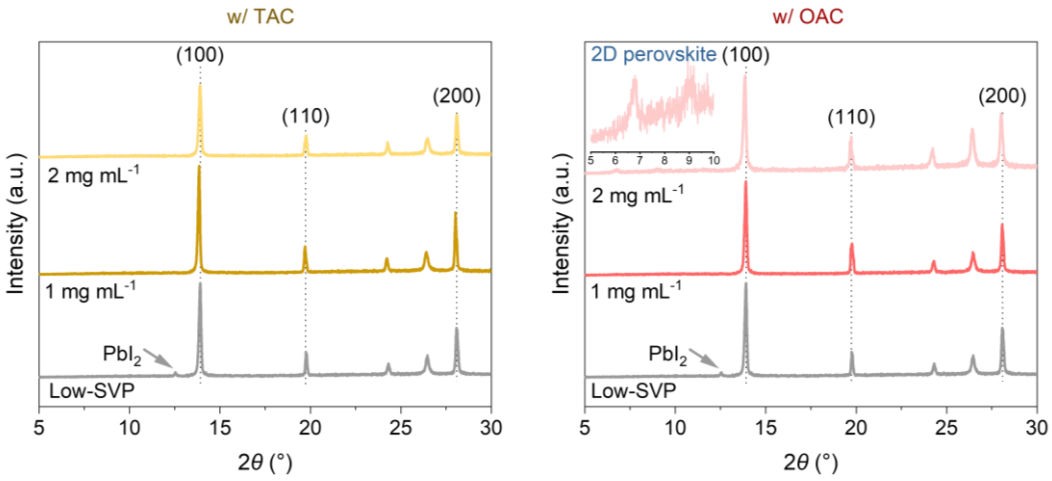

Supplementary Fig. 86 | XRD patterns of perovskite films. Surface characterization was conducted on the top surfaces of low-SVP perovskite films treated with varying concentrations (1 mg mL^{-1} and 2 mg mL^{-1}) of TAC and OAC.

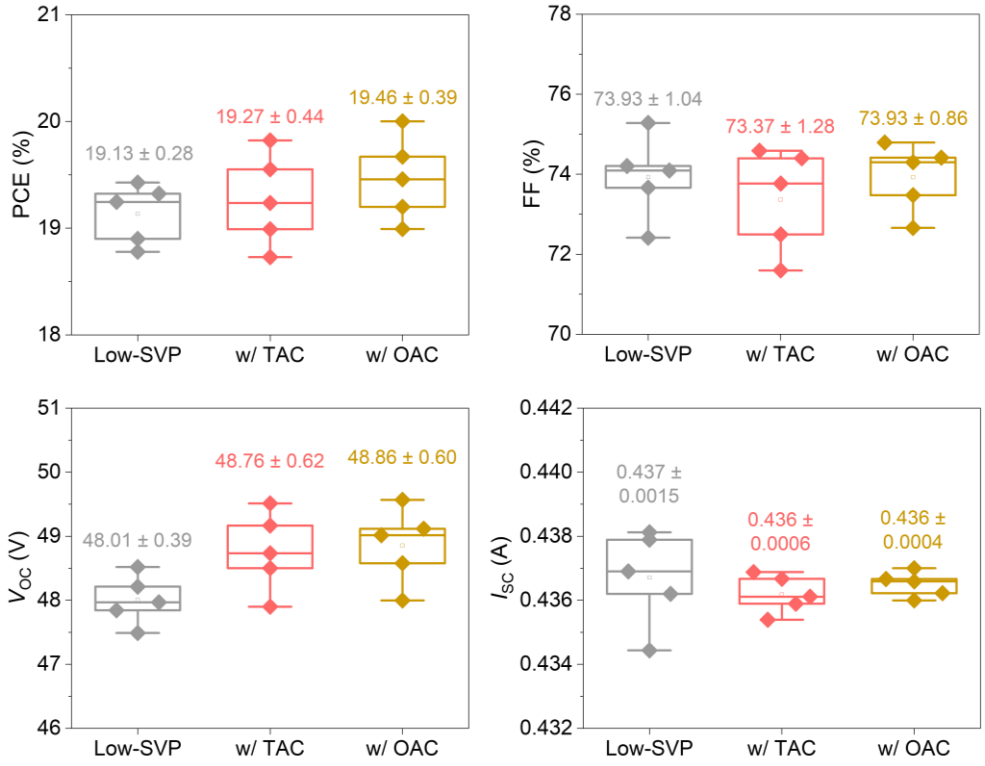

Supplementary Fig. 87 | Statistical photovoltaic parameters of the modules. The PV modules fabricated by low-SVP perovskite films with 1 mg mL^{-1} TAC and 1 mg mL^{-1} OAC. The aperture area of the module is 810 cm^2. Five parallel data sets were taken for each set of conditions. Scatters represent raw data; boxplots show the interquartile range with the median as the center line; whiskers indicate the 5th–95th percentiles. Numerical data are presented as mean ± SD.

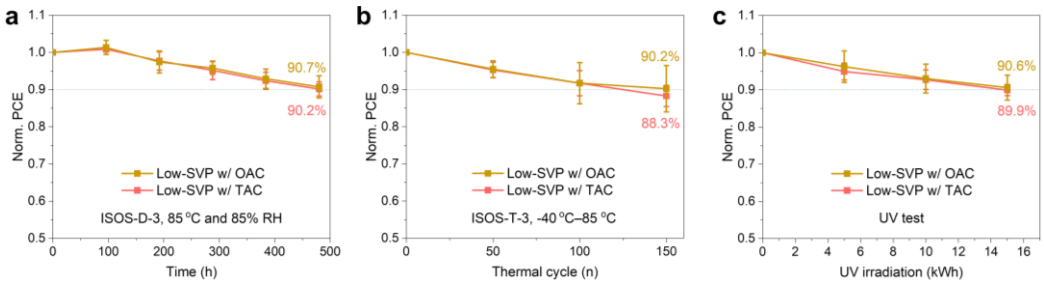

Supplementary Fig. 88 | Reliability tests of 810 cm^2 modules. a, Encapsulated PV modules aged under ISOS-D-3, **b,** ISOS-T-3 testing protocol, and **c,** UV preconditioning test with a cumulative UV irradiation (5 modules for each condition).

6. The proposed reaction mechanism, in which $Pb(OA)_2$ reacts with 2FAI to form 2OA–FA and PbI_2, followed by the reaction of PbI_2 with FAI to form $FAPbI_3$, appears reasonable. However, there seems to be insufficient evidence that nano-sized α-$FAPbI_3$ is formed and that OA passivates both the surface and grain boundaries when $Pb(OA)_2$ is applied to an FAI-rich perovskite film. While changes in the surface are indirectly demonstrated through SEM images and KPFM analysis, evidence regarding changes at grain boundaries appears to be lacking. Therefore, it would be helpful to provide additional analyses focusing on grain boundaries, such as KPFM comparisons between control and target samples.

Response: We appreciate the constructive comments and the recognition of the plausibility of the proposed reaction mechanism, as well as the note regarding the need for more direct evidence concerning α-$FAPbI_3$ formation and $Pb(OA)_2$-mediated grain-boundary passivation. In response, we have conducted TEM characterization to confirm the formation of the α-$FAPbI_3$ phase. Furthermore, we have made extensive efforts to obtain more direct evidence for grain-boundary passivation using various techniques including the KPFM measurements.

We have revised the manuscript and added a detailed discussion in the supplementary information:

"Density functional theory (DFT) calculations indicated that OA^- primarily adsorbs at iodine vacancy sites on the perovskite surface to coordinate with undercoordinated lead, and simultaneously binds to FA^+ cations through hydrogen bonding (Fig. 3b). This adsorption configuration exhibits a higher binding energy than that of I^- at the same sites (Supplementary Fig. 47). The distribution of OA^- in the 3-dimensional depth profile of COO^+, as measured by TOF-SIMS, showed that the oleate was predominantly localized at the film surface, with only trace amounts penetrating into the perovskite bulk via grain boundaries (Supplementary Fig. 48). The measured activation energy (E_a) and cross-sectional potential difference of the perovskite film

confirm that this passivation strategy does not adversely affect ion migration within the film. (Supplementary Note 5, Supplementary Figs. 49–51)."

"*The measured bandgap and transmission electron microscopy of the 3:1 film further confirmed the formation of the α-FAPbI$_3$ (Supplementary Figs. 53 and 54).*"

"***Supplementary Note 5:***

The ion migration activation energy of perovskite film.

Herein, we investigated the ion migration properties of the perovskite films using temperature-dependent conductivity measurements on Au/perovskite/Au structures to experimentally determine the ion migration activation energy (E_a). The activation energy can be extracted by fitting the raw data to the Nernst–Einstein relation:

$$\sigma(T)=\frac{\sigma 0}{T} exp\ (\frac{Ea}{kBT})$$

where σ(T) is the conductivity as a function of temperature, σ0 is a temperature-independent prefactor, and k_B is the Boltzmann constant.

The fitted Arrhenius plots exhibit two distinct linear regimes. In the low-temperature regime, ion migration is essentially suppressed due to insufficient thermal energy. Above a critical temperature, ion migration becomes thermally activated, leading to an exponential enhancement in conductivity.

From the slopes of the Arrhenius plots, the ion migration activation energy of the high-SVP perovskite film was determined to be 0.531 eV, which increased slightly to 0.554 eV after LCP passivation (Supplementary Fig. 49). This small but clear gain in indicates that the LCP passivation strategy moderately suppresses ion migration, a conclusion that aligns with the theoretical calculations presented in Supplementary Fig. 47.

Furthermore, we employed a quasi-in situ FIB-SEM-AFM technique to analyze the cross-sectional morphology and potential distribution. Supplementary Fig. 50a provides a schematic of the sample preparation, Supplementary Fig. 50b shows a photograph of the FIB etching setup, and Supplementary Fig. 50c presents an SEM image of the intermediate layer exposed after FIB etching on the high-SVP perovskite surface. Theoretically, if OA^- were to infiltrate the perovskite bulk along grain boundaries, a potential difference between the grain boundaries and grain interiors would be expected. However, the actual measurements reveal no significant potential contrast between the grain boundaries and the interiors in the micro-region corresponding to Supplementary Fig. 51. We attribute this to the extremely low concentration of OA^- that permeates into the bulk via grain boundaries, resulting in a

negligible change in chemical potential. Additionally, the grain-boundary gaps are highly compact, which may prevent KPFM from accurately resolving the subtle electrical signal variations within such confined areas. Therefore, the trace-level penetration of OA^- does not adversely affect charge transport or the chemical potential landscape within the film."

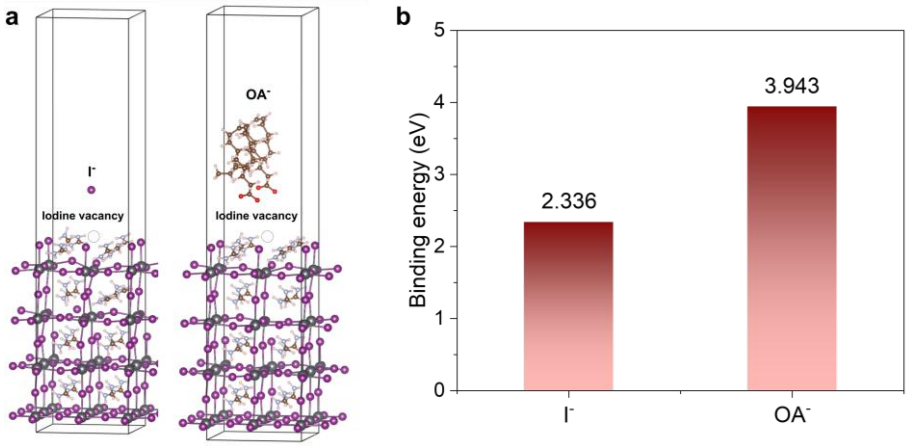

Supplementary Fig. 47 | Calculation of the binding energies of I^- and OA^- at iodine vacancy sites. a, Computational models of I^- and OA^- on a defective PbI-terminated surface (I^- vacancy). **b,** Binding energies of I^- and OA^- occupying iodine vacancies

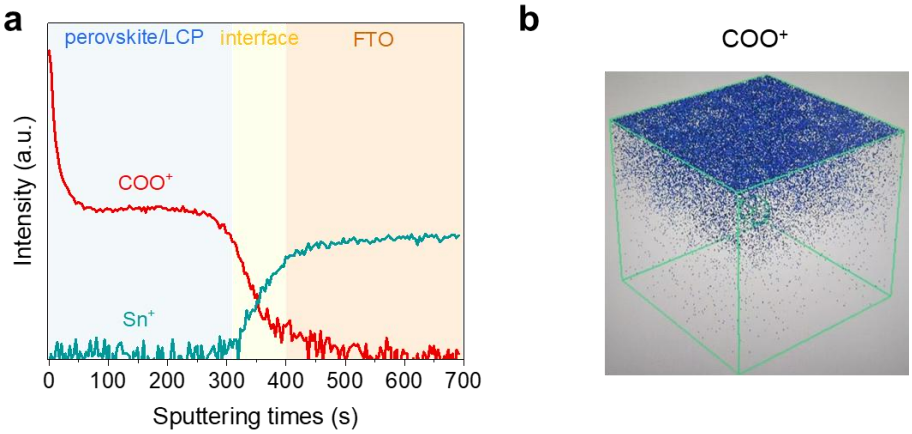

Supplementary Fig. 48 | The TOF-SIMS analysis of high-SVP perovskite film with LCP. a, TOF-SIMS depth profile and **b,** 3D distribution plot of the LCP-passivated perovskite film prepared via the high-SVP method.

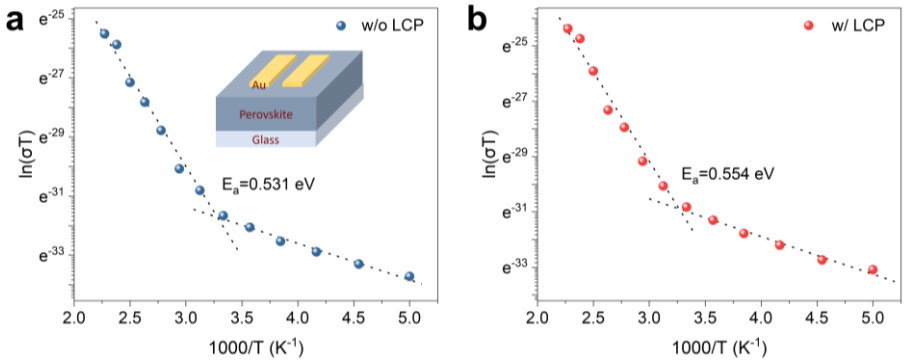

Supplementary Fig. 49 | Temperature-dependent conductivity of perovskite film. a, high-SVP perovskite film and **b,** high-SVP perovskite film w/ LCP.

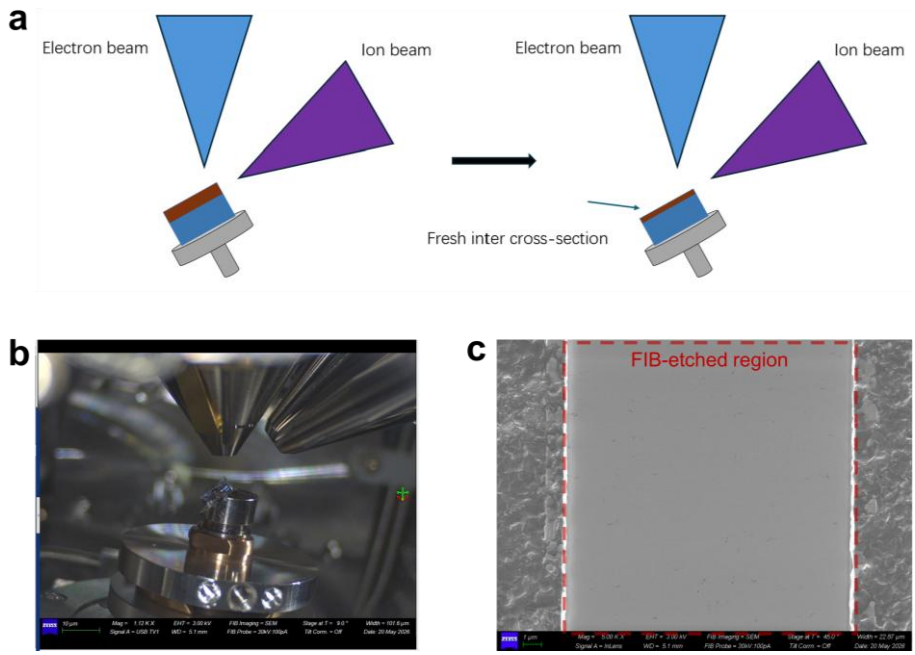

Supplementary Fig. 50 | Surface etching of perovskite film (high-SVP w/ LCP). a, Schematic illustration of focused ion beam (FIB) etching on a perovskite surface. **b,** Photograph of the surface etching setup. **c,** SEM image of the perovskite surface after etching, showing the exposed internal layer where the top surface has been removed in the central region.

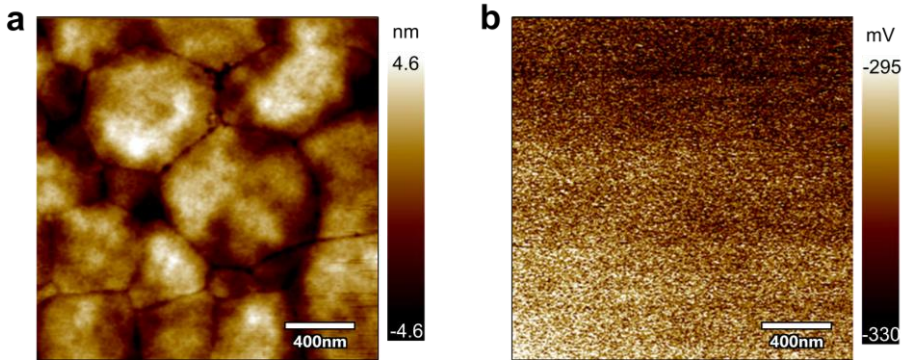

Supplementary Fig. 51 | Potential distribution of perovskite crystals after etching. a, The AFM image and **b,** corresponding KPFM image of high-SVP perovskite film with LCP. The measurement location corresponds to the region subjected to FIB etching in Supplementary Fig. 50c.

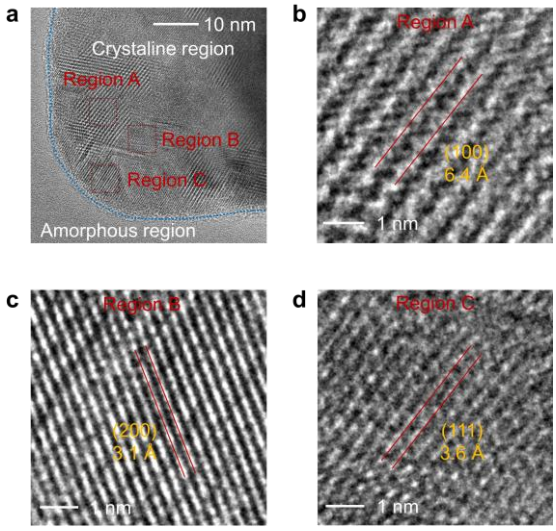

Supplementary Fig. 54 | High-resolution transmission electron microscopy (HR-TEM) images. a, Low-magnification HRTEM image. **b–d,** Magnified HR-TEM images of the regions marked in panel a, corresponding to the (100), (200), and (111) lattice planes of α-$FAPbI_3$, respectively. The sample was fabricated using the same protocol as the LCP:FAI = 1:3 condition in Supplementary Fig. 53, confirming the formation of phase-pure α-$FAPbI_3$.

7. Overall, it appears that both efficiency and durability are improved through the solvent formulation and $Pb(OA)_2$ passivation. It is expected that similar improvements would also be observed at the unit-cell level. For the benefit of readers, it would be helpful to present how the performance of unit devices changes compared to conventional recipes.

Response: We appreciate the positive assessment and constructive suggestion to clarify the performance at the unit-cell level. We have systematically compared the PV parameters of unit cells fabricated using our strategy (high-SVP perovskite w/ LCP) with those prepared via conventional recipes (low-SVP perovskite w/ AHP). The data, now included as Supplementary Note 7, confirm that the efficiency and stability improvements are indeed translated from the module level down to the individual cell level.

"*Moreover, the efficiency and stability trends of the modules closely mirrored those of their constituent unit cells (Supplementary Note 7, Supplementary Figs. 76–82, Supplementary Tables 6–11).*"

"***Supplementary Note 7:***

The performance of the unit cell within the module.

Whether the performance of each unit cell within a module changes in a manner similar to the overall module performance. Here, we compared the relationship between the efficiency of individual unit cells and the overall module efficiency for both high-SVP perovskite modules with LCP passivation and low-SVP perovskite modules with AHP passivation. Furthermore, the modules were subjected to ultraviolet aging under a total solar irradiance of 20 kWh m^{-2}, and the concurrent efficiency degradation of both the unit cells and the modules was analyzed.

To enable simultaneous tracking of individual unit cells within a complete module, we fabricated a perovskite module with an active area of 810 cm^2. Seven independently measurable sub-cells, designated A through G, were interconnected via busbars (Supplementary Fig. 76). To assess operational stability, the modules require encapsulation. Here, we observed a notable phenomenon: after attaching the busbars to the sub-cells and performing high-temperature lamination encapsulation, the efficiencies of both the entire module and the individual sub-cells decrease. We attribute this efficiency loss to the mechanical stress induced by the busbars during the encapsulation process. In the following descriptions, modules before high-temperature lamination are referred to as "unencapsulated," while those after lamination are termed "encapsulated.

The sub-cells in the pristine low-SVP module with AHP passivation are labeled A1 to G1. The full module exhibited an efficiency of 19.32%, while the efficiencies of the individual unit cells ranged from 18.56% to 19.43% (Supplementary Fig. 77 and Supplementary Table 6), indicating inherent performance variations among the sub-cells.

Following encapsulation, both the module and sub-cell efficiencies exhibited a similar declining trend, characterized by a pronounced drop in FF (Supplementary Fig. 78 and Supplementary Table 7). After subsequent UV aging with a cumulative irradiance of 20 kWh m^{-2}, the module efficiency decreased by 17.5%, and the corresponding sub-cells showed synchronized degradation (Supplementary Fig. 79 and Supplementary Table 8), with FF remaining the most severely degraded photovoltaic parameter. For the high-SVP module with LCP passivation, encapsulation also led to an efficiency loss; however, the device still maintained excellent UV stability (Supplementary Figs. 80–82 and Supplementary Tables 9-11). These results indicate that inherent performance variations exist among the sub-cells within a single module, and the degradation observed at the module level is directly mirrored in the individual

sub-cells."

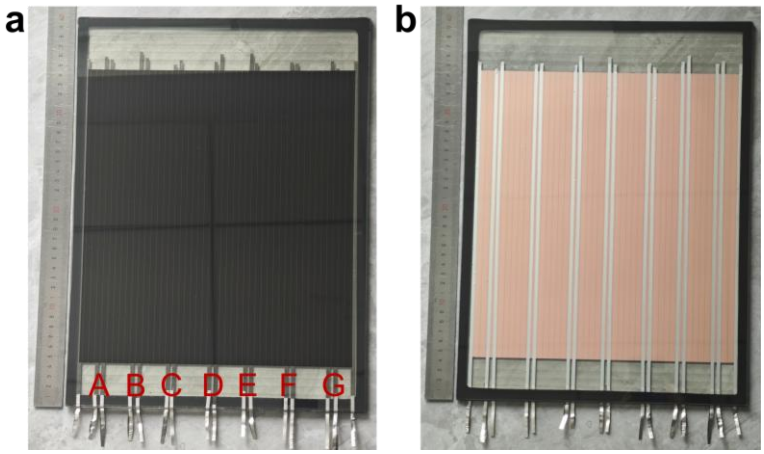

Supplementary Fig. 76 | Image of the perovskite module with an active area of 810 cm^2. a, Front (illuminated) side. **b,** Back (metal electrode) side.

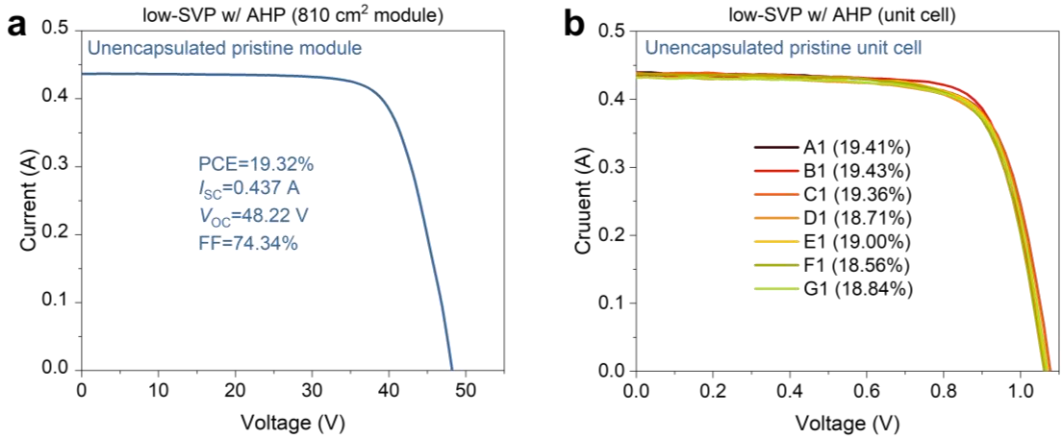

Supplementary Fig. 77 | *I-V* curves of pristine module. a, Unencapsulated 810 cm^2 module fabricated low -SVP perovskite w/ AHP. **b,** The unit cell within AHP module. A1 to G1 denote individual unit cells (A to G) in the low-SVP w/ AHP pristine module, with their spatial positions referenced in Supplementary Fig. 76.

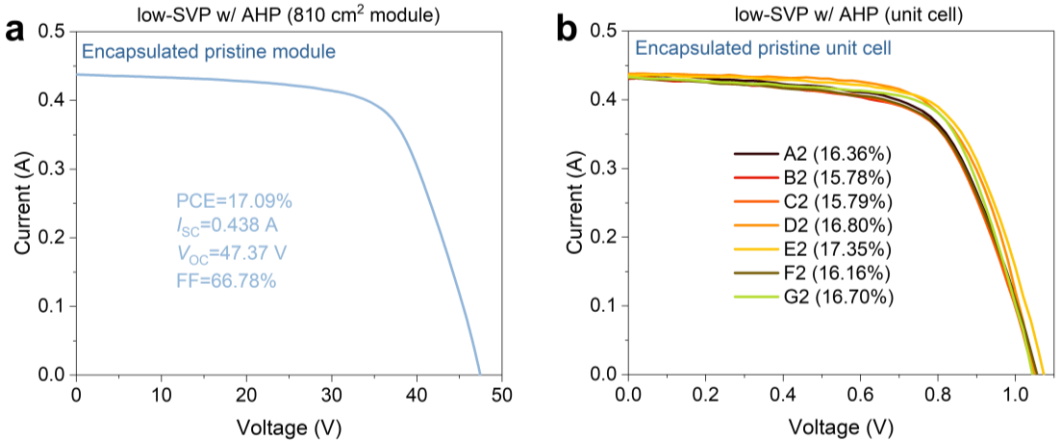

Supplementary Fig. 78 | *I-V* curves of pristine module. a, Encapsulated 810 cm^2

module fabricated low -SVP perovskite w/ AHP. **b,** The unit cell within AHP module. A2 to G2 denote individual unit cells (A to G) in the encapsulated pristine module.

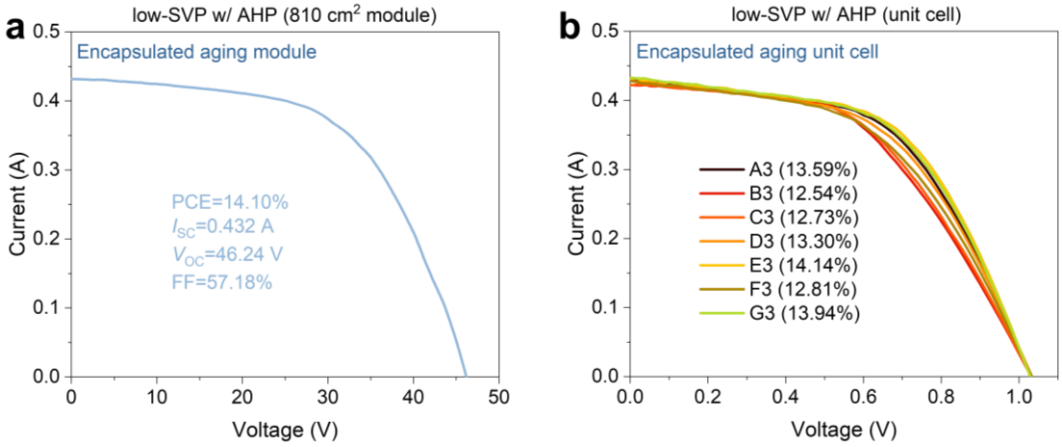

Supplementary Fig. 79 | *I-V* curves of aging module (the cumulative UV irradiation of 20 kWh m^{-2}). a, Encapsulated 810 cm^2 module fabricated low -SVP perovskite w/ AHP. **b,** The unit cell within AHP module. A3 to G3 denote individual unit cells (A to G) in the encapsulated aging module.

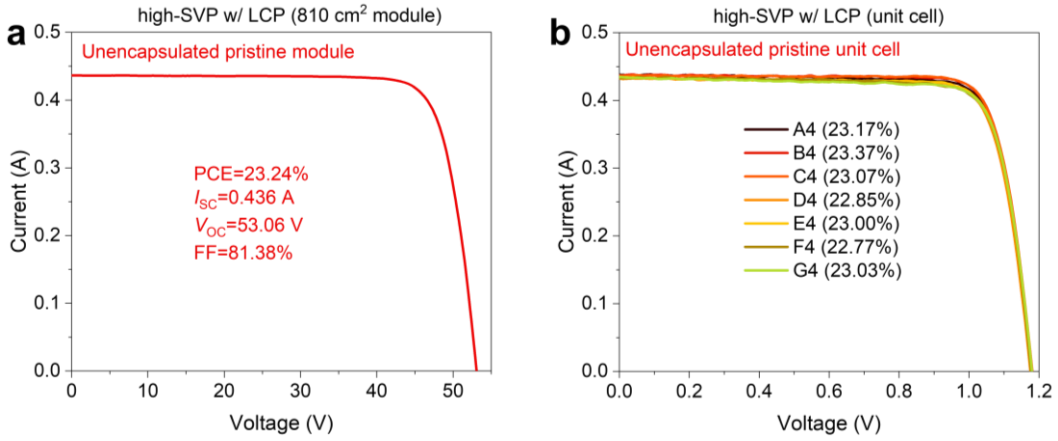

Supplementary Fig. 80 | *I-V* curves of pristine module. a, Unencapsulated 810 cm^2 module fabricated high-SVP perovskite w/ LCP. **b,** The unit cell within LCP module. A4 to G4 denote individual unit cells (A to G) in the high-SVP w/ LCP pristine module.

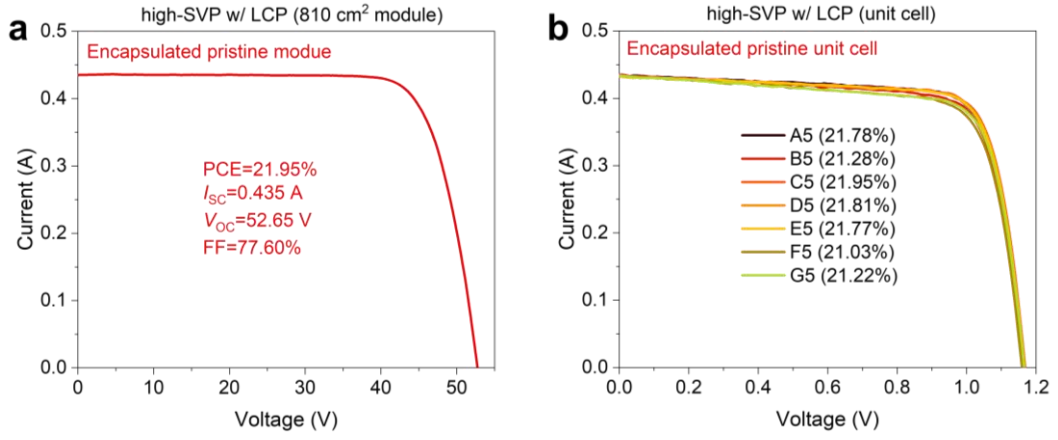

Supplementary Fig. 81 | *I-V* curves of pristine module. a, Encapsulated 810 cm^2 module fabricated high-SVP perovskite w/ LCP. **b,** The unit cell within LCP module. A5 to G5 denote individual unit cells (A to G) in the high-SVP w/ LCP pristine module.

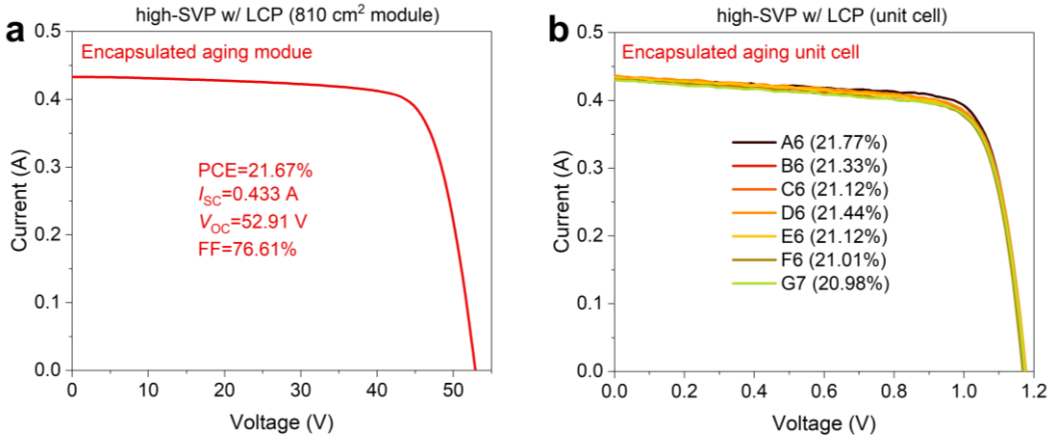

Supplementary Fig. 82 | *I-V* curves of aging module (the cumulative UV irradiation of 20 kWh m^{-2}). a, Encapsulated 810 cm^2 module fabricated high-SVP perovskite w/ LCP. **b,** The unit cell within LCP module. A4 to G4 denote individual unit cells (A to G) in the high-SVP w/ LCP aging module.

Supplementary Table 6. The PV parameters of the unencapsulated pristine unit cells prepared low-SVP perovskite with AHP from *I-V* curves shown in Supplementary Fig. 77.

	I_{SC} (A)	V_{OC} (V)	FF (%)	PCE (%)
A1	0.439	1.077	73.84	19.41
B1	0.436	1.069	75.10	19.43
C1	0.439	1.077	73.68	19.36
D1	0.433	1.068	72.89	18.71
E1	0.437	1.066	73.41	19.00
F1	0.437	1.061	72.03	18.56
G1	0.432	1.068	73.53	18.84

Supplementary Table 7. The PV parameters of the encapsulated pristine unit cells prepared low-SVP perovskite with AHP from *I-V* curves shown in Supplementary Fig. 78.

	I_{SC} (A)	V_{OC} (V)	FF (%)	PCE (%)
A2	0.438	1.056	63.69	16.36
B2	0.431	1.045	63.05	15.78
C2	0.435	1.045	62.57	15.79
D2	0.438	1.049	65.85	16.80
E2	0.436	1.074	66.69	17.35
F2	0.432	1.057	63.69	16.16
G2	0.433	1.045	66.43	16.70

Supplementary Table 8. The PV parameters of the encapsulated aging unit cells prepared low-SVP perovskite with AHP from *I-V* curves shown in Supplementary Fig. 79.

	I_{SC} (A)	V_{OC} (V)	FF (%)	PCE (%)
A3	0.431	1.031	55.02	13.59
B3	0.423	1.031	51.79	12.54
C3	0.422	1.031	52.62	12.73
D3	0.429	1.033	53.96	13.30
E3	0.431	1.028	57.35	14.14
F3	0.428	1.032	52.14	12.81
G3	0.433	1.029	56.36	13.94

Supplementary Table 9. The PV parameters of the unencapsulated pristine unit cells prepared high-SVP perovskite with LCP from *I-V* curves shown in Supplementary Fig. 80.

	I_{SC} (A)	V_{OC} (V)	FF (%)	PCE (%)
A4	0.438	1.177	80.91	23.17
B4	0.437	1.177	81.87	23.37
C4	0.437	1.171	81.24	23.07
D4	0.432	1.175	80.96	22.85
E4	0.433	1.179	80.99	23.00
F4	0.433	1.177	80.44	22.77
G4	0.435	1.180	80.83	23.03

Supplementary Table 10. The PV parameters of the encapsulated pristine unit cells prepared high-SVP perovskite with LCP from *I-V* curves shown in Supplementary Fig. 81.

	I_{SC} (%)	V_{OC} (%)	FF (%)	PCE (%)
A5	0.434	1.165	77.51	21.78
B5	0.435	1.163	75.67	21.28
C5	0.433	1.169	77.99	21.95
D5	0.433	1.166	77.63	21.81
E5	0.433	1.166	77.59	21.77
F5	0.435	1.159	75.10	21.03
G5	0.435	1.166	75.39	21.22

Supplementary Table 11. The PV parameters of the encapsulated aging unit cells prepared high-SVP perovskite with LCP from *I-V* curves shown in Supplementary Fig. 82.

	I_{SC} (A)	V_{OC} (V)	FF (%)	PCE (%)
A6	0.431	1.176	77.25	21.77
B6	0.432	1.175	75.44	21.33
C6	0.431	1.173	75.23	21.12
D6	0.436	1.178	75.09	21.44
E6	0.435	1.176	74.34	21.12
F6	0.430	1.169	75.19	21.01
G6	0.430	1.174	74.89	20.98

8. Finally, in order to enable reproducibility of the experiments, it would be beneficial to provide a more detailed description of the module fabrication process. In addition, it would be helpful to include cross-sectional SEM images as well as SEM images and specifications of P1, P2, and P3 patterning.

Response: We thank the reviewer for the valuable suggestions to enhance the reproducibility and clarity of the module fabrication process. We have added a detailed

discussion and the corresponding experimental data in the revised supplementary information:

"***Supplementary Note 2:***

PV modules fabrication

The fabrication process for the perovskite modules is illustrated in Supplementary Fig. 16, where FTO is fluorine-doped tin oxide, NiO_x is nickel oxide, C_{60} is fullerene, ALD-SnO_2 is atomic layer deposited tin oxide, IZO is indium zinc oxide. Commercial-sized perovskite modules (1.2 m by 0.6 m) were produced on a 150 MW pilot line, following the same processing steps as those established for the 30 cm by 40 cm sub-modules.

First, P1 lines were scribed on a fluorine-doped tin oxide (FTO) glass substrate (30 cm by 40 cm) using a HAN'S LASER system. The substrate was then ultrasonically cleaned sequentially in detergent, deionized water, and isopropanol (IPA), each for 20 minutes. A NiO_x hole-transport layer was subsequently deposited on the cleaned substrate by magnetron sputtering. In ambient air, the perovskite layer was deposited onto the glass/FTO/NiO_x stack via slot-die coating.

For perovskite deposition, the gap between the slot-die coater and the substrate was set to 50 μm, and the coating speed was maintained at 15 mm/s. Immediately after coating, the wet film was transferred to a vacuum-chamber drying (VCD) system, where it was dried for 35 s under a vacuum below 10 Pa. The film was then annealed on a hot plate at 130 °C for 20 min. Prior to slot-die coating, both the ammonium halides passivator (AHP) and lead carboxylates passivator (LCP) solutions were prepared by dissolving the respective materials in IPA.

Next, a 20-nm-thick C_{60} layer was thermally evaporated onto the perovskite film at a rate of 1 Å/s. Approximately 15 nm of SnO_2 was deposited by atomic layer deposition (ALD), followed by the magnetron sputtering of an 80-nm-thick IZO layer. P2 lines were then scribed using the HAN'S LASER system, after which 100-nm-thick Cu electrodes were deposited by magnetron sputtering. P3 lines were scribed with the same laser parameters as those used for P2.

A busbar was attached to the metal electrodes to facilitate electrical testing. The module edges were sealed with butyl rubber, and a polyolefin elastomer (POE) encapsulation film was applied over the active area. A glass cover of the same dimensions as the substrate was placed on top of the butyl rubber and POE stack. The assembly was laminated at 130 °C for 10 minutes. Following lamination, the perovskite solar module was ready for stability testing. Finally, a junction box was installed to

enable series interconnection with adjacent modules, forming a panel suitable for photovoltaic power-station deployment.

A complete perovskite solar module comprises a multilayer stack, as schematically illustrated in Supplementary Fig. 17. Supplementary Fig. 18 also provides cross-sectional schematics of the monolithic interconnection structures defined by the P1, P2, and P3 laser scribes. The widths of the P1, P2, and P3 lines are approximately 29 µm, 69 µm, and 53 µm, respectively, resulting in a dead area width of 158 µm from P1 to P3 (Supplementary Fig. 19). Specifically, the P1 scribe completely isolates the underlying FTO substrate (Supplementary Fig. 20a), while the P2 scribe penetrates through the perovskite layer to make contact with the FTO (Supplementary Fig. 20b). The P3 scribe is terminated at the perovskite surface to isolate the top electrode (Supplementary Fig. 20c). Notably, microscopic curling of the Cu electrode was observed within the P3 scribe lines during the laser process. Furthermore, a cross-sectional SEM image of the fully fabricated module is presented in Supplementary Fig. 20d, confirming the final device architecture of FTO/NiO_x/perovskite/passivator/C_{60}/ALD-SnO_2/IZO/Cu."

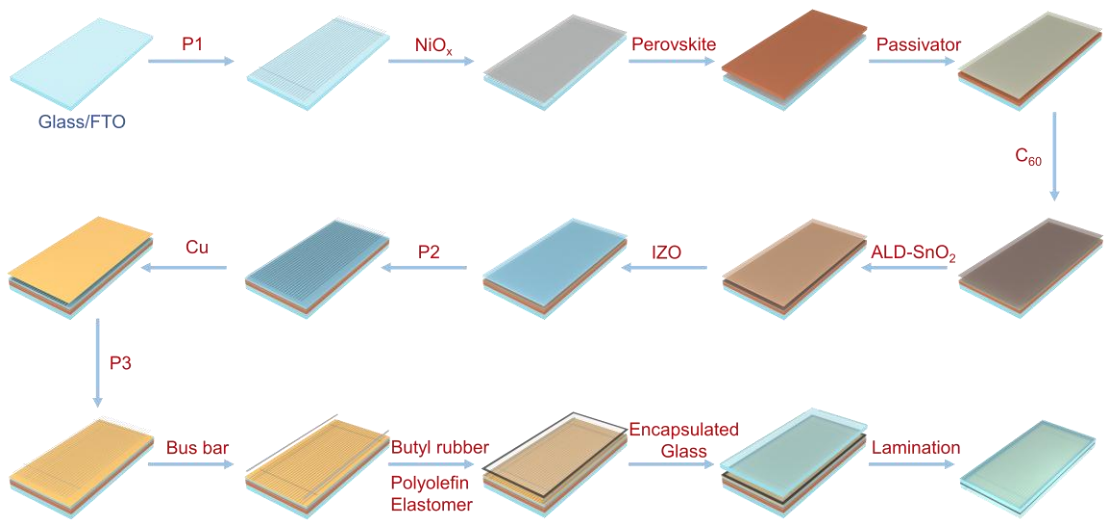

Supplementary Fig. 16 | Process flow diagram for the fabrication of PV modules.

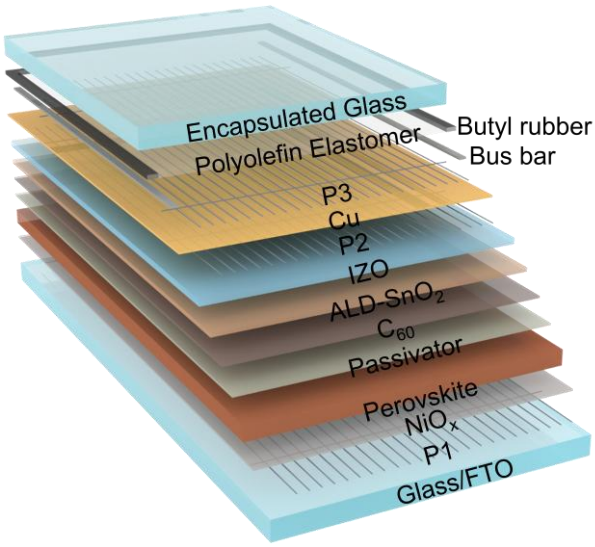

Supplementary Fig. 17 | Configuration diagram of perovskite solar modules.

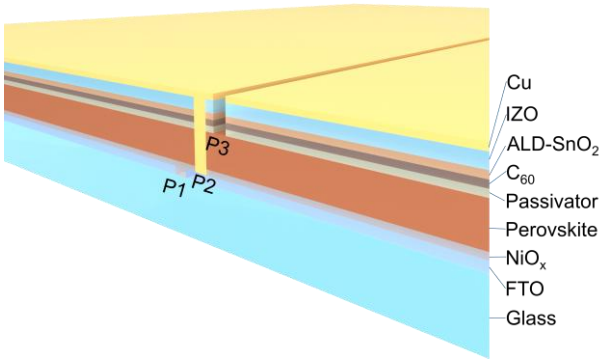

Supplementary Fig. 18 | Cross-sectional schematic of a perovskite solar module showing the P1, P2, and P3 interconnect structures.

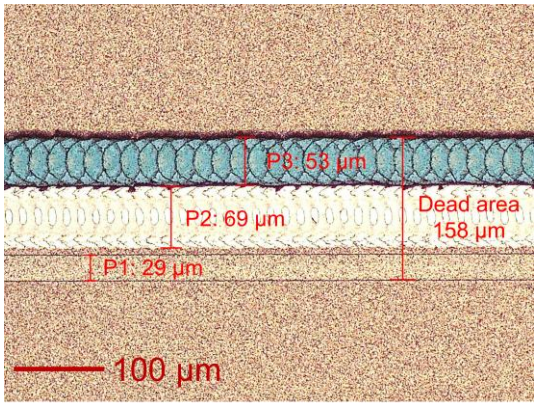

Supplementary Fig. 19 | Microscopic characterization of perovskite solar modules. Optical microscopy image of P1, P2, and P3.

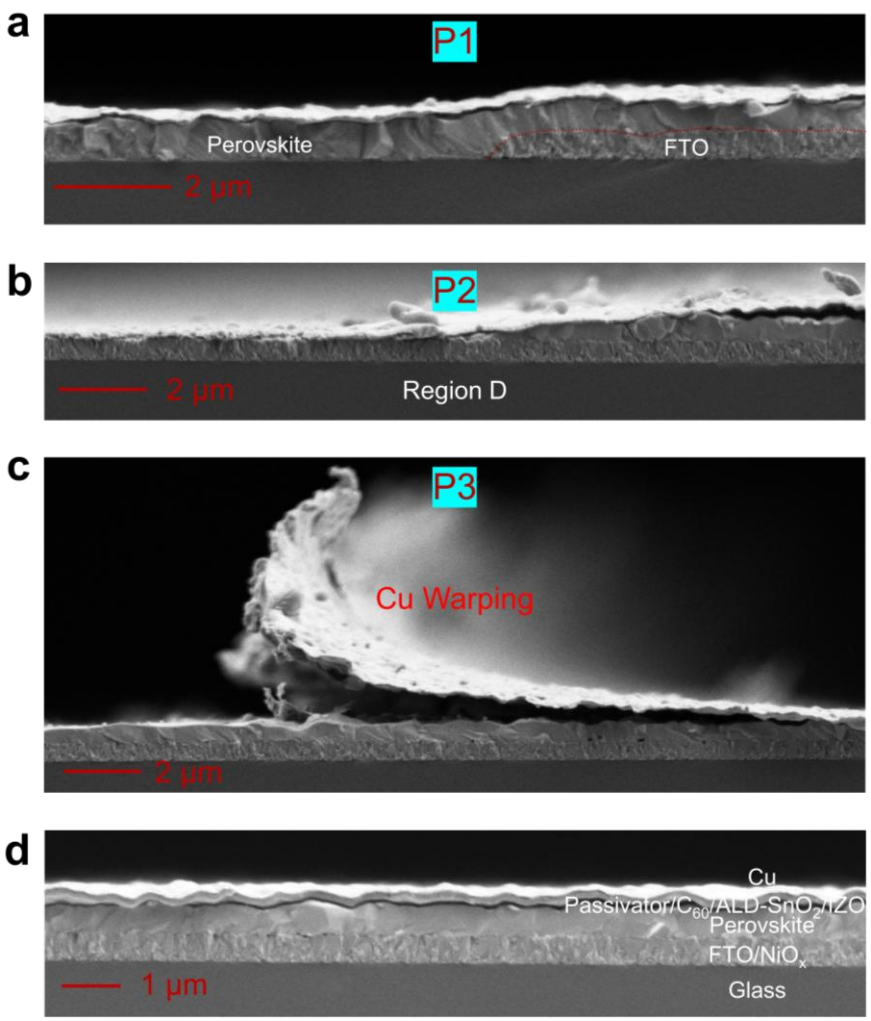

Supplementary Fig. 20 | Microscopic characterization of perovskite solar modules. a-c, SEM cross-sections showing the P1, P2, and P3 interconnects, respectively. **d,** SEM cross-section of the complete module.

Point-to-Point Response to the Reviewers' Comments

Manuscript #: 2026-03-08492A

We thank the reviewers for their positive feedback and for recognizing the significance of this work. We have carefully revised the manuscript according to the comments from the reviewers. Reviewer comments are presented in black, our responses are provided in blue, and the revised text in the manuscript is presented in boxes. All modifications in the revised manuscript have been clearly highlighted.

Referee #1 (Remarks to the Author):

General Remarks

The authors have addressed most of my previous concerns, and I believe that the scientific quality and overall presentation of the manuscript now meet the publication standard of Nature. In my view, this work represents a significant milestone towards highly efficient, stable, and cost-effective perovskite solar modules fabricated entirely using scalable manufacturing techniques. Therefore, I recommend publication in Nature after the authors address the following minor comment.

Response: We sincerely appreciate the positive evaluation of our work. We have carefully considered your remaining comment and have addressed it accordingly in the revised manuscript.

Detailed Comment

The modules presented in this work employ a standalone NiOx hole-transport layer (Supplementary Fig. 16). Given that state-of-the-art perovskite solar cells commonly utilize NiOx/SAM or SAM-based hole-selective contacts to maximize device performance, the authors should clarify the rationale for adopting standalone NiOx in this study and explain why NiOx/SAM or SAM architectures were not pursued. In addition, it would be valuable to discuss the key challenges associated with implementing SAMs in large-area module fabrication and to clarify how this design choice relates to the high module performance reported in this work.

Response: We thank the reviewer for this insightful comment. Indeed, NiO_x/SAM or SAM-based architectures have been widely reported as the preferred hole-selective contact design for achieving high efficiency in state-of-the-art perovskite solar cells (Nature, 2025, 648, 91–96; Nature, 2026, https://doi.org/10.1038/s41586-026-10844-6; Nature Synthesis, 2026, https://doi.org/10.1038/s44160-026-01089-2; Nature Photonics, 2026, 20, 835–842; Science, 2025, 390, 837-842; Science, 2026, 391, eadz7969; Science Advances, 2026, 12, eaeg1456). However, in large-scale fabrication, the volatilization of the solvent tends to result in disordered molecular packing of SAMs, making it difficult to spontaneously form dense and ordered monolayer orientation during slot-die coating. Under such conditions, incomplete coverage and localized disordered stacking of SAMs can severely induce heterogeneous energy level distribution at the interface, thereby impeding efficient charge carrier transport (Joule, 2026, 10, 102390; Advanced Energy Materials, 2026, 16, 2505937; Nature Photonics, 2026, 20, 287–295). Moreover, such disordered stacking can expose a substantial number of phosphonic acid groups toward the perovskite bottom interface, creating reactive sites that promote degradation (Science, 2026, 391, eadz7969). Therefore,

achieving uniform, well-oriented monolayer distribution of SAM materials via slot-die coating may represent an effective pathway toward further improving the performance of commercially viable perovskite modules.

During our initial process exploration, we also conducted extensive trials with these configurations; however, the resulting device efficiencies were consistently unsatisfactory. Consequently, in the present work, we adopted a standalone NiO_x hole-transport layer. That said, we recognize that incorporating NiO_x/SAM or SAM architectures represents a viable and scientifically worthwhile approach for further enhancing the performance of perovskite solar modules.

We now revised manuscript and supplementary information as follows:

"**Supplementary Note 2:**

PV modules fabrication

…

To date, the state-of-the-art architecture typically adopts a TCO/NiO_x/self-assembled monolayer (SAM) or TCO/SAM configuration, in which the SAM is regarded as an essential hole-selective layer for achieving higher-performance perovskite solar cells (p-i-n structure). To further enhance module performance, we also attempted to incorporate SAMs during large-area fabrication. Specifically, we introduced the most commonly used SAM material, (4-(3,6-dimethyl-9H-carbazol-9-yl)butyl)phosphonic acid (Me-4PACz), to construct FTO/NiO_x/SAM and FTO/SAM bottom hole-transport structures. Based on the low-SVP solvent system, perovskite modules with an active area of 810 cm^2 were fabricated following the aforementioned process. As shown in Supplementary Fig. 21, compared with the FTO/NiO_x/perovskite configuration, both the FTO/NiO_x/SAM/perovskite and FTO/SAM/perovskite architectures resulted in lower module efficiencies, primarily reflected in reduced open-circuit voltage (V_{OC}) and fill factor (FF). We attribute this to incomplete coverage and localized disordered stacking of the SAM during large-area slot-die coating, which leads to uneven energy level distribution at the interface and severely impedes efficient charge carrier transport. Due to the critical constraints imposed by uniformity and stability, we excluded SAMs from consideration as the hole transport layer. But adapting SAM materials for commercial perovskite modules to achieve superior photovoltaic performance remains a highly worthwhile research topic. Although our preliminary attempts did not yield effective integration, we will continue to explore this direction in future studies."

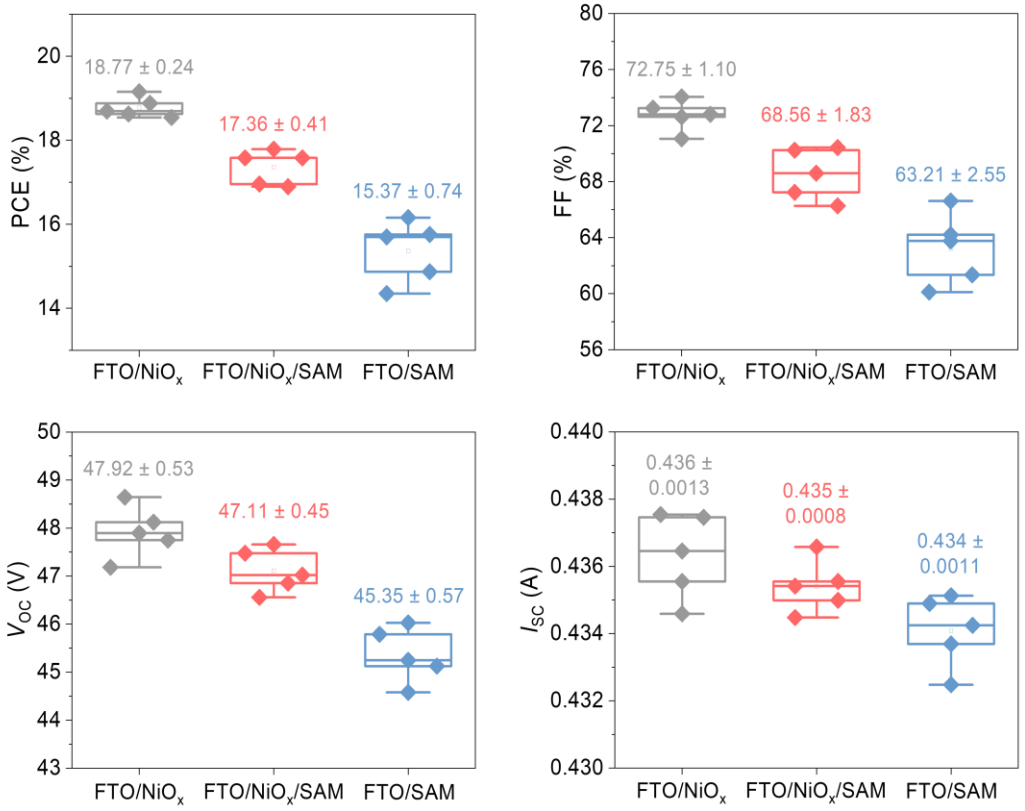

Supplementary Fig. 21 | Statistical photovoltaic parameters of the modules. Perovskite films were fabricated using a low-SVP solvent (DMF:DMSO = 9:1), and none of the modules underwent top-surface passivation. FTO/NiO_x, FTO/NiO_x/SAM, and FTO/SAM denote three different substrates for perovskite coating. The SAM material was dissolved in isopropyl alcohol at a concentration of 0.5 mg mL^{-1}, subsequently deposited by slot-die coating, and annealed on a hot plate at 110 °C for 10 min. The active area of module is 810 cm^2. Five parallel data sets were taken for each set of conditions. Scatters represent raw data; boxplots show the interquartile range with the median as the center line; whiskers indicate the 5th–95th percentiles. Numerical data are presented as mean ± SD.

Referee #2 (Remarks to the Author):

General Remarks

The manuscript has been well revised and it could be accepted as is.

Response: We sincerely appreciate your positive assessment of our revised manuscript and your recommendation for acceptance without further modification. We are grateful for the time and expertise you have devoted to reviewing our work.

Referee #3 (Remarks to the Author):

General Remarks

The authors have thoroughly and satisfactorily addressed all the reviewers' comments and concerns. The revisions made have significantly strengthened the manuscript. In this regard, I recommend this manuscript to be accepted as it is.
(Only one minor correction: In the Nernst–Einstein relation equation, B should be subscript in kB).

Response: We sincerely appreciate for the positive evaluation of our revised manuscript and the careful attention to detail in identifying the typographical error in the Nernst–Einstein relation equation. We have corrected the formatting so that "B" in now appears as a subscript, ensuring consistency with the standard notation.

We now revised manuscript and supplementary information as follows:

"***Supplementary Note 5:***

The ion migration activation energy of perovskite film.

Herein, we investigated the ion migration properties of the perovskite films using temperature-dependent conductivity measurements on Au/perovskite/Au structures to experimentally determine the ion migration activation energy (E_a). The activation energy can be extracted by fitting the raw data to the Nernst–Einstein relation:

$$\sigma(T)=\frac{\sigma 0}{T} exp(\frac{E_a}{k_B T})$$

where σ(T) is the conductivity as a function of temperature, σ0 is a temperature-independent prefactor, and k_B is the Boltzmann constant."